

UC Riverside

UC Riverside Electronic Theses and Dissertations

Title

The Hunt for the Lithosphere-Asthenosphere Boundary in the Southwestern U.S.: A Comparative Study of Sp Receiver Functions and Tectonics, Volcanism, and Seismic Tomography

Permalink

<https://escholarship.org/uc/item/28v0n0wn>

Author

Shallon, Beth

Publication Date

2022

Peer reviewed|Thesis/dissertation

UNIVERSITY OF CALIFORNIA
RIVERSIDE

The Hunt for the Lithosphere-Asthenosphere Boundary in the Southwestern U.S.: A
Comparative Study of Sp Receiver Functions and Tectonics, Volcanism, and Seismic
Tomography

A Thesis submitted in partial satisfaction
of the requirements for the degree of

Master of Science
in
Earth and Planetary Sciences

by

Beth M. Shallon

June 2022

Thesis Committee:

Dr. Heather A. Ford, Chairperson
Dr. Maryjo Brounce
Dr. Gareth Funning

The Thesis of Beth M. Shallon is approved:

Committee Chairperson

University of California, Riverside

ACKNOWLEDGEMENTS

I would first like to thank my thesis advisor, Dr. Heather A. Ford, who helped me navigate this first step in my graduate education. Her genuine enthusiasm and ongoing curiosity for the work we do has been an inspiration and motivation through the challenges that arise in research. I am extremely grateful to have learned and grown as a researcher under her guidance for the past two years, and am excited for the opportunity to continue to learn from her for my Ph.D.

Second, I would like to thank the whole Earth and Planetary Sciences Department at the University of California Riverside, both faculty and fellow graduate students. I have gained an incredible amount of information both in and out of the classroom in my time here that would not have been possible without the people in this department.

Lastly, I would like to thank my family for their continued support throughout all of my education. My parents have always encouraged me to follow my interests, and they helped me establish the work ethic that got me to where I am today. And my brother continually pushed me to exceed my own expectations of what I could accomplish in my coursework and research by reminding me to go back to basic concepts when things did not go to plan.

ABSTRACT OF THE THESIS

The Hunt for the Lithosphere-Asthenosphere Boundary in the Southwestern U.S.: A Comparative Study of Sp Receiver Functions and Tectonics, Volcanism, and Seismic Tomography

By

Beth M. Shallon

Master of Science, Graduate Program in Earth and Planetary Sciences
University of California, Riverside, June 2022
Dr. Heather A. Ford, Chairperson

Lithospheric thickness in the western United States has been found to be thinner than that of the stable continental interior of North America. Explanations for this thin lithosphere range from active tectonics to the presence of partial melt. Importantly, the western U.S. has been used to argue for a relationship between lithospheric thickness and thermotectonic age. Past studies of Sp receiver functions and tomography models in the western U.S. have led to significant improvements in our understanding of mantle structure and related dynamic and tectonic processes, but significant uncertainty remains as the results have yet to be successfully integrated. In our analysis we calculated Sp receiver functions using data from over 1000 broadband stations from more than 50 temporary and permanent networks, ranging from 31°N to 43°N and 112°W to 126°W. The average depth of the lithosphere-asthenosphere boundary (LAB) phase across the region in our study is 65.3 km, but absolute depths vary from roughly 30 to 100 km. In this study we take a systemic approach to generating maps of the seismic lithosphere-asthenosphere boundary inferred from Sp

receiver functions and compare them to a commonly used map of physiographic provinces and sections, volcanic centers, and the surface wave tomography model of Shen and Ritzwoller (2016) to assess if, and to what extent, our interpretation of the lithosphere-asthenosphere boundary is consistent with these different models and observables. Comparison of our results to the tomography model reveal good agreement between receiver function LAB depth and the absolute depth range between maximum and minimum velocities in the tomography model, suggesting that receiver functions are in fact imaging the lithosphere-asthenosphere boundary. However, little detailed agreement exists between them, likely due to differences in sensitivity. Comparison of LAB depth to our tectonic proxies yields little correlation and we find that the relationship between physiographic boundaries does not appear to extend to variations in lithospheric thickness in the mantle. Preliminary comparisons between petrologic studies and our picks reveal minimal agreement in LAB depth, but we find variation in LAB depth between volcanic centers when compared to non-volcanic areas.

TABLE OF CONTENTS

Introduction	1
Tectonic Setting	5
Data and Methods	9
Receiver Function Overview	9
Data	10
Phase Picking	11
Rotation and Deconvolution	11
Stacking	13
Results	14
General Description of Results and Phase Selection	14
Regional Comparisons	19
Pacific Border Province	24
Cascade-Sierra Mountain Province	26
Basin and Range Province	27
Colorado Plateau Province	28
Columbia Plateau Province	28
Discussion	29
Negative Phase Interpretation	29
Physiographic Dependence of the LAB	32
Volcanic Controls on the LAB	35
Tomography as a Constraint on the LAB	39
Conclusion	45
References	48

LIST OF FIGURES

Figure 1: Lithosphere and Boundary Layer Types	56
Figure 2: Map of Volcanism in Southwestern US	57
Figure 3: Province Map of Fenneman and Johnson (1946)	58
Figure 4: Station Map	59
Figure 5: Data Coverage Map	60
Figure 6: Map of Example Single Station Stacks	61
Figure 7: Example Single Station Stacks	62
Figure 8: Map of Cross Section Locations	66
Figure 9: Latitudinal Cross Sections	67
Figure 10: Longitudinal Cross Sections	70
Figure 11: Hand-picked LAB Maps	72
Figure 12: Auto-picked LAB Map	74
Figure 13: Pacific Border Province Histograms	75
Figure 14: Cascade-Sierra Mountains Province Histograms	76
Figure 15: Basin and Range Province Histograms	77
Figure 16: Colorado Plateau Province Histograms	78
Figure 17: Columbia Plateau Province Histograms	79
Figure 18: LAB Maps of Big Pine & Coso Volcanic Fields	80
Figure 19: LAB Volcanic Center Map Comparison	81
Figure 20: Volcanic Center Histograms	82
Figure 21: Tomography Model of Shen and Ritzwoller (2016)	84
Figure 22: Tomography Versus Receiver Functions	85
Figure 23: Wave Speed Versus Receiver Functions	86

LIST OF TABLES

Table 1: LAB Depth Characteristics by Physiographic Province	87
Table 2: LAB Average Amplitudes by Physiographic Province	88
Table 3: LAB Depth Characteristics for Volcanic Regions	89

Introduction

The Earth can be subdivided into layers based on chemical composition (i.e., crust, mantle, core) or by mechanical properties. The mechanical layering of the Earth distinguishes the inner (solid) and outer (liquid) core and extends outward, subdividing the mantle into several layers, including the mesosphere (lower mantle), asthenosphere (upper mantle), and the lithosphere (uppermost mantle and crust). It is commonly held that the lithosphere is defined as a rigid layer consisting of the crust and uppermost mantle that moves atop the weaker, lower viscosity asthenosphere below it (e.g., Artemieva, 2011). The properties responsible for causing the mechanical differences between the lithosphere and the asthenosphere are frequently debated, although it is thought that changes in temperature, pressure, water, and/or melt content may all play a role (e.g., Fischer et al., 2010). This debate is due in part to observational limitations and variations in sensitivities between methods, as well as differences in discipline-specific definitions of the lithosphere-asthenosphere system (Artemieva, 2011; Eaton et al., 2006). For example, seismic lithosphere, thermal lithosphere, petrological lithosphere, electrical lithosphere, and elastic lithosphere (Figure 1) all have distinct definitions based on the physical, compositional, or mechanical properties being constrained.

The transition from lithosphere to asthenosphere is commonly referred to as the lithosphere-asthenosphere boundary, or LAB, and references to lithospheric thickness are commonly, but not always, treated as being synonymous with LAB depth. The LAB can be defined as one or more types of boundary layers: mechanical, thermal, rheological, and

chemical. Figure 1 demonstrates the connections between different definitions of lithosphere and the various boundary layer types. The elastic lithosphere is defined as a mechanically coherent plate and is constrained by gravity and surface topography (Artemieva, 2011) and the mechanical boundary layer (MBL) is defined as the boundary separating the elastic lithosphere from the underlying asthenosphere. The thermal boundary layer (TBL) definition is based on the dominant mode of heat transfer within a layer – the lithosphere is thought to be dominated by conductive heat transfer and the asthenosphere is dominated by convective heat transfer (Sleep, 2005). The thickness of the thermal lithosphere can be constrained from seismic, thermal, petrologic (xenolith), electromagnetic, and magnetotelluric data (Artemieva, 2011; Porter & Reid, 2021). Seismic imaging methods can be used to help constrain the depth of the rheological boundary layer (RBL) view of the LAB, where the asthenosphere is thought to be a layer with reduced viscosities and enhanced mantle flow (Artemieva, 2011). Seismic imaging methods can also be used to help constrain the petrologic lithosphere, which is defined as being depleted in FeO relative to MgO (i.e., has a higher olivine Mg#) relative to the (lower olivine Mg#) asthenosphere (Griffin et al., 2004; Lee et al., 2009) as seismic velocities are sensitive to changes in iron content (Lee, 2003).

For this study, we focus on the seismically defined lithosphere-asthenosphere boundary. The seismic lithosphere is commonly defined as the high velocity lid above a low velocity asthenosphere (Forsyth, 1975). Numerous seismic methods exist for imaging the seismic LAB, but these approaches often lead to different results. For seismic tomography models,

proxies such as the depth of the most rapid negative velocity gradient (Debayle & Kennett, 2000; Li et al., 2003) or absolute velocity perturbation relative to a reference model with depth (Li & Burke, 2006) are examples of approaches used to define the base of the lithosphere (or LAB). Anisotropy in surface waves can be used to determine the depth of the base of the lithosphere by finding changes in orientation of mantle fabrics produced by shearing at the base of the plate (e.g., Nettles and Dziewonski, 2008). Perhaps the most common method for determining the depth of the LAB is through receiver functions, which rely on seismic wave conversions occurring at seismic discontinuities within the Earth (Rondenay 2009; Rychert et al., 2007), and which we discuss in more detail in the methods section. We note that each of these seismic methods have different sensitivities to seismic structure (Eaton et al., 2006; Fischer et al., 2010), which can result in differences in measured LAB properties, including depth to the boundary and velocity gradient across the boundary. Significant differences can exist when comparing receiver functions to surface wave tomography results. Surface wave velocity is controlled by the average velocity over a broad range of depths. Therefore, sharp velocity contrasts – such as the base of the tectonic plate – can be misinterpreted as a small variation over a large depth. In contrast, converted phases identify depths at which sharp seismic velocity contrasts occur; however, the amplitude of a converted phase only allows the relative velocity contrast to be inferred (Joe Byrnes, personal communication).

No matter which seismic approach is utilized, the depth at which the LAB is found on Earth varies globally and such variations appear to be correlated with tectonic age. More

specifically, the thickness of the lithosphere tends to increase with tectonic age (Romanowicz, 2009; Schaeffer & Lebedev, 2013) and is typically observed to be thickest under old, stable parts of continents (i.e., cratons) and thinnest in ocean basins or tectonically active continental regions (Fischer et al., 2010). In ocean basins, a model in which the thickness of the lithosphere corresponds with heat flow from the surface of the oceanic plate, in accordance with a half-space cooling plate model (Nettles and Dziewonski, 2008; Nishimura & Forsyth, 1989). Beneath the continental U.S., differences in lithospheric thickness estimates can also be attributed to differences in thermotectonic age (Porter et al., 2019). In many instances, receiver function estimates of LAB depth are consistent with surface wave estimates, such as beneath the western U.S. (e.g., Abt et al., 2010; Levander & Miller, 2012) or eastern Australia (Birkey et al., 2021; Ford et al., 2010). In other instances, significant differences between imaging methods are found. For example, Fishwick (2010) observed that the estimated depth of the LAB from receiver functions in central and southern Africa differed by approximately 50-100 km from surface wave tomography estimates.

In this study we present an updated set of images of the seismic discontinuity structure beneath the western U.S. using S_p receiver functions, expanding upon the work of Ford et al. (2014) and Lekic et al. (2011). We use our S_p receiver function results to generate maps of estimated LAB depth and amplitude using a simple framework and compare these results to a commonly used model of physiographic provinces (Fenneman, 1931) to better understand the extent to which lithospheric properties and tectonics agree. We also explore

the relationship between volcanic locations and lithospheric properties at three volcanic centers- Lassen, Mammoth Mountain, and Salton Buttes. Lastly, we perform a preliminary analysis comparing our results to the ambient noise surface wave tomography model of Shen and Ritzwoller (2016) to understand the extent to which receiver functions agree with tomography models beneath the western U.S., a region where initial, qualitative comparisons suggest there should be agreement.

Tectonic Setting

In this study we focus on the tectonically active western U.S., centered on California and Nevada, spanning an area from the Pacific coast to east of the Great Salt Lake ($\sim 112^\circ$ W), and the northern edge of the Gulf of California ($\sim 31^\circ$ N) northward to the Craters of the Moon National Park ($\sim 43^\circ$ N). We focus on this region in part because (1) the tectonic history is well-studied, (2) seismic data is abundant and readily available, (3) qualitative agreement exists between numerous tomography models and previously published receiver function results and (4) because the LAB gradient is thought to be relatively sharp (Abt et al., 2010), making it a suitable target for receiver function analysis. More generally, the region is host to a complex and evolving plate boundary with elements of extension (e.g., Gulf of California, Basin and Range Province), transform plate motion along the San Andreas fault system and subduction of the Juan de Fuca slab beneath North America in the Pacific Northwest (Faulds & Henry, 2008). Prior to the existence of the transform plate boundary, the Farallon plate was subducting beneath the North American plate, resulting in an extended period of magmatic activity beneath the western margin of North America

(Atwater, 1970; Putirka et al., 2012). During the Eocene (~40 Ma), the Farallon plate began to fragment into microplates, including the Juan de Fuca and Monterey plates, and by ~28 Ma the motions of these microplates were largely decoupled from each other (Atwater, 1989). Around the same time (i.e., ~30 Ma), the San Andreas fault system began forming a dextral strike-slip fault between the Pacific and North American plates where a section of the Farallon plate had completely subducted (Nicholson et al., 1994). The Monterey plate was captured by the Pacific plate when the spreading center stalled ~18 Ma, thus extending the length of the transform boundary between the Pacific and North American plate (Atwater & Stock, 1998). After the capture of the Monterey microplate, the motion along the transform margin caused the rotation of the western Transverse Ranges and extreme extension beneath the Inner Borderlands (Nicholson et al., 1994). Widespread extension in the Basin and Range began at ~17-16 Ma (Camp et al., 2015) and between ~13-6 Ma the transform system jumped inland from the west coast of Baja California (Stock & Hodges, 1989). Extension in the Gulf of California began at ~12 Ma, but the combination of dextral and extensional motion for Baja California to reach its present-day position may not have been achieved until ~6 – 7 million years later (Oskin et al., 2001).

Today, the transform plate boundary between the Pacific and North American plates consists of over 1,000 km of an interconnected, regionally extensive system of faults that accommodate right lateral motion (Faulds & Henry, 2008). The transform boundary begins in the north at the Mendocino Triple Junction at ~40°N and comes onshore in California at ~39°N. North of the Mendocino Triple Junction, the Juan de Fuca plate is subducting

beneath the North American plate (Faulds & Henry, 2008). In southern California, the transform motion terminates near the Salton Sea ($\sim 33^{\circ}\text{N}$), and changes to extensional motion which continues through the Gulf of California. Global plate-circuit solutions indicate that the North American and Pacific plates are moving relative to each other at a rate of ~ 52 mm/yr (Atwater & Stock, 1998). However, the San Andreas does not move as a rigid system, as some of the faults exhibit stick-slip motion while others exhibit creep (Beeler et al., 2001). Furthermore, roughly 20% of the motion between the North American and Pacific plates is accommodated off the plate boundary (i.e., in the Eastern California Shear Zone and Walker Lane), so seismicity is also common throughout eastern California (Stevens et al., 2013).

In addition to tectonic activity, the landscape of the western U.S. has been heavily modified by volcanism since the onset of magmatism associated with the subduction of the Farallon. Some of the volcanism is much more recent, as can be seen in Figure 2, which shows the ages calculated for volcanic samples in the region (data from NAVDAT). These samples span much of the region, but closely follow the locations of the known volcanic centers (Figure 2). The young volcanism north of 40°N and at a longitude of roughly 122°W is largely due to the subduction of the Juan de Fuca plate (Atwater, 1970), east of this is volcanism associated with the High Lava Plains, Snake River Plain and corresponding Yellowstone hot spot. Much of the remainder of recent volcanism borders the Basin and Range, with a significant number of volcanic centers found along the present-day Sierra Nevada and nearby Walker Lane, Eastern California Shear Zone and Mojave regions. A

young trend of volcanic centers also extends northward near the western edge of the Colorado Plateau and southward along the Colorado Extensional Corridor (e.g., Feuerbach et al., 1993). Volcanism in the Pacific Northwest is largely due to subduction, while the origin of the High Lava Plains is debated and may be associated with hot spot activity further east (Hopper et al., 2014). Multiple explanations for the numerous volcanic centers exist elsewhere but are too numerous to discuss here. In regions such as eastern California, the abundance of magmatism may be the result of the lingering effects of the subduction (Putirka et al., 2012), extension in the Basin and Range (Putirka & Platt, 2012) or foundering of the Sierra Nevada Batholith (Gazel et al., 2012).

For the ease of dividing this region into tectonic domains, we will be using the physiographic provinces presented by Fenneman (1931) (Figure 3). The model is based on commonalities in topography, rock types and structure, and geologic and geomorphic history. It should be noted that these provinces were first described prior to the establishment of plate tectonic theory, however they continue to be used in seismic imaging studies to delineate tectonic domains used in discussion (e.g., Yuan et al., 2011). The naming convention established by Fenneman (1931) has physiographic divisions, of which there are 8 in the contiguous United States; physiographic provinces, that total to 25 across the contiguous states; and physiographic sections, which total to 76. In the region of interest, there are 8 physiographic provinces from 3 different physiographic divisions, with a total of 20 physiographic sections. In Figure 3, each physiographic section is given a

different shade of the color assigned to its province (i.e., Basin and Range sections are browns, Pacific Border sections are green).

Data and Methods

Receiver Function Overview

Receiver functions (RFs) are time or depth series of seismic structure beneath a seismometer that are computed by removing the effects of the source and instrument response (Wilson et al., 2006) from teleseismic phase arrivals. The two common types of RFs used to study receiver side structure are Ps and Sp. Although the two methods are conceptually and practically similar, there are fundamental differences between the two that limit their application and interpretation. It is generally accepted that Ps RFs are better for imaging crustal structure (e.g., Lekic et al., 2011; Wilson et al., 2006) and mantle transition zone structure (e.g., Ba et al., 2019), as Sp RFs have lower resolution than Ps RFs (Liu & Shearer, 2021). Furthermore, Sp RFs are generated from a more limited epicentral range than Ps RFs to avoid postcritical phases (Abt et al., 2010), and Sp waveforms typically have lower signal-to-noise ratios due to larger relative noise levels (Krueger et al., 2021). However, Sp RFs are considered better suited for imaging upper mantle structure such as the LAB, since Ps RFs are often contaminated with later P arrivals from crustal reverberations in the time window of LAB scattered Ps arrivals (Rychert et al., 2007; Wilson et al., 2006). Sp receiver function analysis has become widely used to characterize LAB structure in a range of tectonic environments from stable continental interiors (e.g., Birkey et al., 2021; Krueger et al., 2021) to passive margins (e.g., Ainsworth

et al., 2014), from rift zones (Lavayssiere et al., 2018) to well established spreading centers (Rychert et al., 2014) and regions of active subduction (Possee et al., 2021).

Data

We searched the USGS National Earthquake Information Center (NEIC) global event catalogue for events greater than magnitude 5.8 and between epicentral distances 30° and 90° and generated a list of over 10,000 events which occurred between depths of 0 km and 1000 km during the period from January 1980 to April 2021. For our subsequent Sp receiver function analysis, we further reduced the number of events used to those that with epicentral distances between 55° and 75° , and had a maximum depth of 300 km. These epicentral limits were imposed because Sp phases are not generated at mantle discontinuities for distances less than $\sim 55^\circ$, and to avoid potential interference from SKS and SKSp phases at distances greater than 75° (Ford et al., 2010). Furthermore, the maximum phase depth was limited to 300 km to avoid possible interference from P-wave multiples (Abt et al., 2010). Restricting stations to latitude bounds of 31°N to 43°N and longitude bounds of 112°W to 126°W and using our reduced list of events from the NEIC, we collected waveform data from the Incorporated Research Institute for Seismology (IRIS) Data Management Center (DMC) for all available short-term and long-term seismic stations. In total, over 1000 broadband stations from over 50 networks (Figure 4) were used in our analysis.

Phase Picking

To prepare the data for processing, we initially rotated the waveforms from north and east components to vertical and radial components. The phase arrivals were automatically picked via a process originally described in Abt et al. (2010). This process predicts the arrival times of direct P and S waves by finding the peak value of the signal-to-noise ratio of the absolute value of the Hilbert transform of the filtered wave, after convolving it with the Hanning window. For comparison, we used the TauP toolkit to predict the arrival time of the direct P and S arrivals for the 1-D model AK135 (Crotwell et al., 1999; Kennett et al. 1995). After using both methods to determine the expected arrival times of the direct P and S waves, waveforms were removed if the arrival times between the signal-to-noise pick and the TauP predicted arrival were more than 5 seconds apart.

Rotation and Deconvolution

An essential step in the calculation of receiver functions is the deconvolution of two or more seismograms for a given station-event pair. The aim of this deconvolution is to remove source and instrument response while retaining information on structure beneath the receiver. Before deconvolution, we transformed the north and east components to P and SV. The rotation into the P-SV-SH reference frame is important as the incidence angle of the incoming seismic waves is not generally perpendicular relative to the Earth's surface, resulting in the propagation of P and S energy on both horizontal and vertical components (Abt et al., 2010; Li et al., 2007). To complete this rotation, we searched for the combination of compressional (V_p) and shear (V_s) wave velocities that minimize the

energy of the parent wave (P for Ps; S for Sp) on the daughter component (SV or SH for Ps; P for Sp) in a short window around the phase arrival for each event at a station via the free-surface transfer matrix (Abt et al., 2010; Bostock, 1998)

$$\begin{bmatrix} P \\ SV \\ SH \end{bmatrix} = \begin{bmatrix} \frac{(\beta^2 p^2 - 1/2)}{\alpha q_\alpha} & \frac{p\beta^2}{\alpha} & 0 \\ p\beta & \frac{(1/2 - \beta^2 p^2)}{\beta p_\beta} & 0 \\ 0 & 0 & 1/2 \end{bmatrix} \begin{bmatrix} Z \\ R \\ T \end{bmatrix}$$

where α is the near surface compressional velocity and β is the near surface shear velocity, p is the ray parameter of the direct phase, $q_\alpha = \sqrt{\alpha^{-2} - p^2}$, and $q_\beta = \sqrt{\beta^{-2} - p^2}$. We then determined which combination of velocities provided the best overall reduction in parent phase energy on the daughter component for all event-station pairs, and re-rotated all events at the station using this combination of V_p and V_s . For Sp receiver functions, the window used in this analysis was centered around the S phase arrival (from our S2N pick, discussed earlier – see Phase Picking) and was extended to 75 seconds before and 25 seconds after the direct S arrival.

Prior to deconvolving, waveforms were bandpass filtered (0.03-0.5 Hz for Sp), normalized by the maximum amplitude of the parent component and weighted according to the parent phase signal-to-noise, and we apply a 0.5 s cosine taper to the parent component before the phase arrival (Abt et al., 2010). We then performed an extended-time multi-taper cross-correlation deconvolution for each source-receiver pair to obtain individual Sp receiver functions. This process is described in Lekic et al. (2011) and implements the

deconvolution methodology described in Helffrich (2006) to improve on the multi-taper frequency domain cross-correlation deconvolution from Park and Levin (2000). The extended-time multi-taper deconvolution method is a more stable deconvolution method than the water level frequency domain approach of Abt et al. (2010) and allows us to calculate single event-station pairs suitable for common conversion point stacking.

Stacking

Individual receiver functions were stacked in two different ways, by station, and by common conversion point (CCP). Both were migrated using the one-dimensional model, AK135 (Kennett et al., 1995). Although the use of the model AK135 may result in small differences in absolute depth of the interpreted lithosphere-asthenosphere boundary relative to a more accurate 3D model (e.g., Ford et al., 2014), both Lekic et al. (2011) and Abt et al. (2010) found differences to be negligible when using a 1D model instead of a 3D model. Individual receiver functions stacked beneath a given station can help to provide a detailed view of the velocity structure with depth beneath that station. However, single station stacks only provide information about the structure beneath one location and do not account for 3D variations in seismic structure (Rondenay, 2009). Common Conversion Point (CCP) stacks allow us to generate more detailed receiver function images that vary as a function of latitude, longitude, and depth. In our analysis we stacked over a volume that is discretized by 0.1° in latitude and longitude, and 0.5 km in depth. At each point in the volume, CCP stacks were calculated by taking a weighted average of all the receiver functions in the region. The weighting factor used in our study was a normalized cubic

spline representative of a simplification of the Fresnel zone of Sp converted phases (Lekic et al., 2011). This helped us to account for finite frequency effects not accounted for in simple ray theory (Lekic & Fischer, 2017). For example, the weighting factor gave full weight to rays that fell directly on a discretized point within our volume, half weight to rays within a quarter wavelength (of S waves assuming their dominant period), and no weight to anything beyond (Lekic et al., 2011). Figure 5 illustrates the weighted number of waveforms used at each point in our CCP stacked results at a depth of 70 km.

For both the single station and CCP stacked results, we bootstrapped our data 100 to determine the robustness of individual phases. Through bootstrapping, some events were sampled multiple times in a single iteration, while others were not sampled at all. We saved the 100 iterations, and calculated both the standard deviation and the mean of the receiver functions. The results shown in the following sections represent the mean of the bootstrapped receiver functions, for both the single station and CCP stacks. Two standard deviations are plotted in the single station results and the corresponding uncertainties are used in the selection of the negative phases in the CCP stacks, discussed in later sections.

Results

General Description of Results and Phase Selection

Sp receiver functions are commonly used to image mantle discontinuities because they avoid contamination from crustal reverberations present in Ps receiver function analysis (Kind et al., 2012; Lekic et al., 2011) and are better able to image horizontal interfaces than

body or surface wave tomography (Bostock, 1998; Fischer et al., 2010). In both the single station results (Figures 6 & 7) and in the common conversion point stacks (Figures 8, 9, & 10) that we present in this paper, red shaded regions correspond to positive phases, which are inferred to represent a velocity increase with depth (i.e., positive velocity gradient). In the western U.S. positive phases at depths of ~15-45 km are typically interpreted to be the crust-mantle boundary (Moho), although they can also result from positive velocity gradients located within the crust, due to structures such as basins (Liu et al., 2018). The largest observed positive phase in our results is typically observed at depths of less than 50 km, which we interpret to be the Moho. However, we caution that this interpretation is not done carefully and believe that Ps receiver function analysis is better suited for such analysis due to its better depth resolution (Wilson et al., 2006). In our images, blue shaded regions correspond to negative phases, which result from a velocity decrease with depth (i.e., negative velocity gradient). In the western U.S., negative phases at depths of ~50-100 km are most frequently correlated with the lithosphere-asthenosphere boundary (LAB) (e.g., Levander & Miller, 2012). We note that the velocity decrease across the LAB is unlikely to be an instantaneous change, and both the depth range over which the velocity change occurs (gradient thickness), along with the velocity contrast across the boundary, impacts the amplitude of the negative phase (Rychert et al., 2007). The larger the gradient thickness, or the smaller the velocity contrast across the boundary, the weaker the amplitude of the negative phase in the receiver function (Lekic et al. 2011). Understanding the degree of velocity change across the LAB has important implications for constraining which of the physical and chemical properties are changing. For example, both Rychert et

al. (2007) and Ford et al. (2010) demonstrated that melt must be present in the asthenosphere in order to explain the RF amplitudes in their respective study areas. The largest amplitude negative phases that we observe vary in depth, amplitude, and degree of continuity. For example, while the negative phase in some parts of our study area appears as a nearly continuous feature with small variations in depth and amplitude (e.g., cross section D-D', 116°W-114°W; Figure 9), in other areas the negative phase exhibits more complex behavior with larger variations in amplitude and depth (e.g., cross section A-A', 123°W, 120°W-118°W; Figure 9). Furthermore, in some regions we observe multiple negative phases of similar amplitude at a given location (cross sections B-B', 124°W-123°W; F-F', 116°W-115°W; G-G', 40°N-39°N; I-I', 34°N-33°N; Figures 9 & 10), and sometimes sandwich a smaller positive phase between them.

The criteria for selecting the negative phase in a receiver function are critical in the workflow for inferring what the phases may represent in terms of seismic structure. In our analysis of the CCP stacked results, we introduce a simple, systematic method for picking negative phases. First, we assert that the negative phase must exist below the first statistically significant positive phase located at assumed Moho depths (10 to 45 km). That is, the transition from lithosphere to asthenosphere can be no shallower than the Moho as the crust is considered to be part of the lithosphere. Second, the negative phase is the single largest negative phase beneath this Moho phase located at depths of 120 km or less. This lower depth criterion is based on qualitative estimates of lithospheric thickness from tomography models for the region (Schmandt & Humphreys, 2010). Later in our study we

perform a quantitative analysis of the robustness of this assumption. Third, this single largest observed negative phase must also be statistically significant based on uncertainty estimates from bootstrapping. In our analysis, statistical significance is given to any phase for which the two standard deviations exceed a threshold of zero (above zero for positive phases, below zero for negative phases). If all these criteria are not met for a given latitude and longitude bin, no pick is made. It is important to note that in picking these phases, no assumptions were being made about the structure they represent – the negative phases at this point in our analysis simply represent a velocity decrease with increasing depth in the mantle. For many of the receiver functions, there were additional negative phases. These secondary negative phases can be seen in the single station stack for stations like CI.SMM, XD.A35, and TA.W12A (Figure 6) and the CCP cross sections B-B', F-F', G-G', and I-I' (Figures 9 & 10). Secondary negative phases are likely robust structural features; however, our analysis is focused on testing a simplified framework of Sp RF interpretation, and future work will look to more sophisticated picking methods and the implications of phase multiplicity. Furthermore, we report the depths of the negative phase to tenths of a kilometer for the purpose of discussion of results, however, this is beyond the vertical depth uncertainty of ± 10 km of receiver functions (Ford et al., 2014).

Using the method described above, negative phases were selected across our CCP stacks. The depth of the negative phase ranges from 35.7 km to 107.4 km (Figure 11), with an average of 65.3 km. The amplitude of this phase ranges from 0.02 to 0.2 (Figure 11), with an average of 0.07. The picked phase depths and amplitudes are variable throughout the

region, with the depths typically changing more rapidly, and exhibiting more lateral heterogeneity, than the amplitudes. Some regions have smaller perturbations in the selected depth phase (cross section D-D', 122°W-120°W; cross section I-I', 41°N-38°N), while other areas have large lateral offsets in negative phase depth (greater than 20 km; cross sections B-B', 120°W-119°W, 116°W-115°W; F-F', 120°W-118°W, 116°W-115°W; Figures 9 & 10). Previous studies that focused on California found the average depth of the negative phase to be 70 km (Ford et al., 2014; Lekic et al., 2011), however, our average is approximately 5 km shallower and is likely due to the inclusion of the Basin and Range in our study. Examples of regions with shallower-than-average negative phase depths include, but are not limited to, areas such as the Inner Borderlands and the Salton Trough, both of which are well documented regions of thinning (Ford et al., 2014; Lekic et al., 2011), as well as a particularly shallow region in central southern Nevada, which was also seen by Hopper and Fischer (2018) (Figure 11). Examples of regions with deeper-than-average negative phase depths include the northern non-volcanic part of Nevada (slightly north of the Great Salt Lake in Utah), and a region just north of the California-Oregon border (Figure 11).

We also used an automated picking function to select the negative phase based on the largest negative phase in the depth range 30-150 km, smoothed with a Gaussian function (Figure 12). The auto-picking algorithm does not consider whether the negative phases are well resolved, but instead limits picks to those phases with an amplitude greater than 0.04. An identical version of this same picking algorithm was used in Ford et al. (2014) and

Lekic et al. (2011), which is why we choose to include it in our study. The auto-picking function yielded an average depth of 65.3 km for the negative phase over our study area, a value identical to our hand-picking method. In general, good agreement exists between the hand-picked and auto-picked negative phase depths, with only small differences due to smoothing and the absence of picks in regions with lower amplitudes such as in the southern half of California where amplitudes are smallest and fall below the 0.04 cut-off (Figure 11). The automated picking algorithm also generated more negative phase picks along the edges of the data set, where uncertainties may be larger due to the limited number of events, however further analysis is needed to understand this difference. Due to the similarity between the hand-picked and auto-picked phase depths and the greater coverage of the hand-picked phases, we will focus our remaining discussion on the hand-picked results.

Regional Comparisons

To assist us in the discussion of our results we rely on the physiographic provinces of Fenneman and Johnson (1946) (Figure 3). Outlines of the physiographic provinces of the western U.S. are often included in the overview of regional seismic studies of mantle structure (e.g., Levander & Miller, 2012; Yuan et al., 2011). While not explicitly discussed in such studies, the use of such boundaries is predicated on the idea that the provinces are a proxy for the generalized geology and tectonics of the region. However, these physiographic provinces are based on the morphology and geology of a landscape, rather than a specific tectonic framework, and predate plate tectonic theory. Ultimately, it is

unclear to what extent variations in physiography may reflect the current state of mantle lithosphere. We use these physiographic provinces to discuss our results and perform comparative studies across our study area, while acknowledging the very real limitations of such an approach.

To begin our analysis of negative phase variability in relation to physiographic provinces, we randomly sampled single station stacks to look at the structure beneath specific stations in each province (Figure 6). This approach is akin to work done before the Transportable Array component of EarthScope, when continental scale studies were limited to single station analyses (e.g., Abt et al., 2010; Li et al., 2007). No criteria were used in determining which stations to look at, however, we did seek to sample stations from each province in order to gauge variability. Figure 7 displays this sampling of single station stacks in order of longitude from west to east. The number of waveforms used to calculate the stacks varied from 15 waveforms at XE.SNP86 in the Sierra Nevada section to 415 waveforms at CL.SNCC in the Los Angeles Ranges section. For all the stations, the largest negative amplitude phase was marked with a solid cyan horizontal line (Figure 7). Shallow depth (i.e., <60 km depth) picks of the negative phase exist at stations XQ.ME24 (California Trough), CL.SNCC (Los Angeles Ranges), XC.OR087 (Harney), and XF.FEAR (Salton Trough). Deeper picks for the negative phase depth (i.e., >80 km depth) exist at stations XQ.ME10 (Klamath Mountains), TA.L04A (Southern Cascade Mountains), 8E.MB04 (Sierra Nevada), TA.W12A (Sonoran Desert), AE.U15A (Grand Canyon), and UU.MTPU (High Plateaus of Utah).

In our cross sections, the physiographic provinces are color coded at the top of each profile according to Figure 3. For example, the Great Basin is prominently featured in light brown in cross sections B-B', C-C', D-D' and I-I' and J-J' (Figures 9 & 10). Generally speaking, the negative phase within the Great Basin is larger in amplitude than beneath most of California (Figure 11) and is remarkably consistent in depth in some regions (cross section I-I', 41°N-38°N), in agreement with other studies (Hopper & Fischer, 2018; Lekic & Fischer, 2014). A deeper negative phase exists beneath the Los Angeles Ranges (light green; cross sections F-F', H-H', I-I') and in the Middle Cascade Mountains (dark red; cross section A-A'), while shallower negative phase exists beneath the Salton Trough (dark brown; cross sections F-F', J-J'), in good agreement with previous studies (Lekic et al., 2011).

Although general trends in the behavior of the negative phase can be discerned from the cross sections, we sought quantitative measures for the variability of the phase (e.g., changes in depth or amplitude) in each of the provinces to understand the extent to which physiographic provinces and sections may correlate with mantle structure. Table 1 contains all the physiographic provinces which have values for the picked negative phase. The colors in the table correspond to the general grouping of colors used for each province and set of sections (Figure 3). The values listed as unbootstrapped in Table 1 (“Average Depth”, “Maximum Depth”, “Minimum Depth” and “Depth Range”) are the negative phase depths taken from the data set, with the average calculated as the mean of the depth within each

section. It is important to note that the number of depth points is the total number of possible values for the negative phase that might have been picked based on the bounds of each physiographic section; however, this includes NaNs, which represent locations where we were unable to pick a depth of the lithosphere-asthenosphere boundary and were not used in calculating the average depth. The columns under “Bootstrapped Values” are for average depths that have been bootstrapped. In this case, we resample the negative phase depths in each section, calculating the average depth of the negative phase repeatedly over 100 iterations. In the case of the “Bootstrapped Values”, “average_B depth” refers to the average of averages, taken over the 100 iterations, “Maximum_B” and “Minimum_B” depths represent the minimum and maximum bootstrapped average depths calculated over the 100 iterations, and “Depth Range_B” is the difference between the maximum_B and minimum_B.

In most of the physiographic sections, the bootstrapping did not result in an average_B depth different from the (unbootstrapped) average depth. The greatest difference between the two averages occurred in the Lower Californian province for which the average_B depth was 0.3 km deeper than the average depth. Unless otherwise specified, all discussion of average depths throughout the remainder of the paper are in reference to the unbootstrapped average depths. However, where we do observe variations in the bootstrapped phase depths is in the depth range_B. Here, the magnitude of the depth range_B of bootstrapped values appears to correspond to the variability of the (unbootstrapped) phase depths within each section. For example, the Sierra Nevada and Klamath Mountains Sections have similar maximum phase depths of 95.3 km and 98.8 km (respectively), and minimum phase depths of 46.0

km and 49.3 km (respectively), producing similar depth ranges of 49.3 km and 49.5 km (respectively) and average depths of 65.3 km and 68.1 km (respectively). However, the depth range_B for the Sierra Nevada is 1.1 km, while for Klamath Mountains it is 3.0 km. While the difference between these values appears small, upon inspection of the histogram phase depths (Figures 13 & 14) for each section, we see that the depth values are distributed differently. For the Sierra Nevada Section the vast majority of the phase depths fall within a range of a roughly 15 km centered around 65 km (Figure 14), while in the Klamath Mountains Section there appears to be a bimodal distribution of phase depths centered at depths of roughly 55 km and 75 km (Figure 13). In sections 4.3-4.7 we further describe the features of the negative phase in several different provinces.

In terms of amplitude, much of southern and central California have amplitudes with absolute values of less than 0.06 for the picked negative phase, with no apparent change relative to any particular tectonic or physiographic boundaries. East and north of California, the amplitudes commonly exceed values of 0.06, with values easily passing 0.08 in most regions (Figure 11). Similarly to the case for the average negative phase depth calculation, the average amplitude of the negative phase was calculated within each physiographic section, or province if there are no sections, by taking the mean of all the non-NaN amplitude values for the region. The average amplitude of the negative phase was also bootstrapped over 100 times. Table 2 displays the average amplitude and average bootstrapped amplitudes (amplitude_B) grouped by physiographic province. All sections, and provinces, have the same value for the average amplitude and average bootstrapped

amplitude_B, except for the Klamath Mountains Section in the Pacific Border Province, which has a 0.01 difference between the two. The smallest average amplitude is 0.04, in the Pacific Border Province for the California Trough and Los Angeles Ranges Sections. The largest average amplitude of 0.11 is seen in the Walla Walla Plateau Section of the Columbia Plateau Province. The second largest average amplitude is 0.10 in the Grand Canyon Section (Colorado Plateau Province) and the Oregon Coast Ranges Section (Pacific Border Province). An average amplitude of 0.06 is found in four sections and two provinces: High Plateaus of Utah (Colorado Plateau), Sonoran Desert (Basin and Range), Sierra Nevada (Cascade-Sierra Mountains), California Coast Ranges (Pacific Border), Lower Californian, and Middle Rocky Mountains. Although some of the provinces can be grouped together by amplitude of the negative phase pick, the variations in amplitude do not appear to systematically correspond to physiographic boundaries. Ford et al. (2014) found an increase in the amplitude of the negative phase moving east of the San Andreas Fault, but we do not see this change. While we are not sure of the cause, these differences could be due to changes in methodology between the two studies. Such differences include the use of different corner frequencies in filtering the data, an updated approach to phase picking, and the inclusion of bootstrapping, which was not included in Ford et al. (2014). Future work will focus on understanding the differences between the two studies.

Pacific Border Province

The Pacific Border Province is comprised of the coastline sections including (from north to south) the Oregon Coast Ranges, Klamath Mountains, California Coast Ranges, and the

Los Angeles Ranges. It also includes the California Trough, which is more commonly referred to as the Central Valley. The Pacific Border Province consists of a chain of coastal mountain ranges, differing in age (i.e., Klamath Mountains are Paleozoic, Los Angeles Ranges are Cenozoic) and orientation, with inland valleys (Fenneman, 1931). In the Pacific Border Province, average depths range from 57.0 km to 68.1 km (Table 1). The Oregon Coast Ranges are not included in further discussion due to insufficient data. The Klamath Mountains Section has the deepest average negative phase out of the Pacific Border Provinces with an average negative phase depth value of 68.1 km. The California Coast Ranges Section has the shallowest average negative phase depth of the province at 60.7 km. In each of these sections the depth phases appear to be, to differing extents, bimodally distributed (Figure 13). This bimodal distribution is best illustrated in the Klamath Mountains (depth range_B = 3.0 km), where two distinct populations of phase depths appear, and to a lesser extent the California Trough (depth range_B = 4.0 km). The bimodal behavior is less pronounced in the California Coast (depth range_B = 2.0 km) and Los Angeles Ranges (depth range_B = 2.4 km). In the Los Angeles Ranges the majority of the phase depths are centered around the average depth of 67.1 km, however a small tail centered at 40 km also exists. This small tail corresponds to the well-resolved shallow negative phase observed beneath the Inner Borderland in previous studies (Ford et al., 2014; Lekic et al., 2011) and is thought to be the result of extensive lithospheric thinning due to extension of the Inner Borderland during rotation of the Western Transverse Ranges (Lekic et al., 2011).

Cascade-Sierra Mountains Province

The Cascade-Sierra Mountain Province is a quasilinear chain of inland mountain ranges that run north-to-south within our study area and includes the currently active arc volcanoes of the Middle and Southern Cascade Mountains to the north, and the Cretaceous-aged Sierra Nevada batholith to the south (Stevens et al., 2013). The section with the greatest average negative phase depth in the entire study region is the Middle Cascade Mountains Section, with an average negative phase depth of 84.9 km. This contrasts with the Southern Cascade Mountains, which has one of the shallowest average negative phase depths of our study, with an average of 55.7 km. The third physiographic section in this province, the Sierra Nevada Section, has an average negative phase depth of 65.3 km (Table 1).

The calculated depth ranges_B of the three sections vary considerably, with a study maximum of 11.3 km beneath the Middle Cascades; however, depth distributions of the Middle Cascades are not shown due to insufficient data since it is on the edge of the region, raising the possibility that the ranges_B of 11.3 km may be due to insufficient data and not a function of variations in seismic structure. The Southern Cascade Mountains have a calculated depth range_B of 3.6 km, which stems from negative phase depths clustered at 50-55 km, 57-60 km and 65 km (Figure 14). While this absolute range of depths is small, the clear multimodal clustering is a compelling feature that we plan to study more carefully in the future. In contrast, the Sierra Nevada Section displays a strong convergence of the negative phase depths around the section average (Figure 14). The consistency of the

negative phase depth along the Sierra Nevada has previously been documented by Ford et al. (2014), although they found values for the negative phase ~5-10 km deeper than we do here.

Basin and Range Province

The province with the most consistency in negative phase depth within its physiographic sections is the Basin and Range Province. Extension in the Basin and Range Province has been occurring at varying rates since the Miocene (Camp et al., 2015), and volcanism has occurred predominantly in the southwest of the province at irregular intervals throughout the Cenozoic (Fenneman, 1931). Although the depth of the negative phase in this province varies from a minimum of 35.7 km in the Salton Trough to a maximum of 107.4 km in the Great Basin, the average negative phase depths for each section are within 5-6 km of each other. The greatest average depth belongs to the Great Basin, with an average depth of 66.6 km, and the shallowest average depth belongs to the Salton Trough, with an average depth of 60.9 km (Table 1). With the exception of the Salton Trough, the sections have a low depth range_B value, consistent with negative phases centered around the average, although there is still considerable variability of negative phase depths within the distributions (Figure 15). The Salton Trough Section displays two distinct negative phase depths centered at less than 40 km and more than 60 km, consistent with prior Sp imaging results of the region (Lekic et al., 2011).

Colorado Plateau Province

The province containing sections that sees the most changes from the average depth to the average_B depth is in the Colorado Plateau. The Colorado Plateau Province is identifiable by its coherently uplifted strata to elevations greater than 1.5 km (Fenneman, 1931). Although we show four sections of the Colorado Plateau in Figure 3, only three of these sections have depth picks for the negative phase. Both the High Plateaus of Utah and Grand Canyon sections see a 0.1 km increase in average_B depth of the negative phase after bootstrapping, meanwhile the Navajo section has a 0.1 km decrease in the average_B depth after bootstrapping (Table 1). The High Plateaus of Utah contain one of the deepest picks of the negative phase at 107.3 km, with the largest number of depth picks falling in the 80 – 90 km range. The average_B phase depth for the High Plateaus of Utah is 81.5 km, falling within the confidence interval ranging from 80.1 km to 82.9 km (Figure 16). The Grand Canyon has two groupings of depth values (one >65 km, one <65 km), in which the one at greater depth has a larger population. Therefore, the bootstrapping process condensed the average depth distribution to converge at nearly the same depth of 67.7 km, however, the range of potential depths to expect the negative phase has decreased to 1.7 km (Figure 16).

Columbia Plateau Province

Our study samples the southern half of the Columbia Plateau Province, which includes (from west to east) a sliver of the Walla Walla Plateau, Harney, Payette and Snake River Plain Sections. The Columbia Plateau Province has experienced large lava flows which

define the region, but the sections within the province differ in altitude and topography (i.e., the Snake River Plain is exemplary of a lava plain, Payette is a mix of mountains and lava plateaus, Harney is a basin; Fenneman, 1931). Average negative phase depths vary from 49.8 km (Walla Walla Plateau) to 66.3 km (Snake River Plain; Table 1). Similar to the Pacific Border Province, the sections within the Columbia Plateau Province display variable depth ranges_B. The Walla Walla Plateau has a calculated depth range of zero owing to the lack of data in the bin, while both the Payette and Snake River Plain sections have relatively large calculated depth ranges_B of 3.0 km and 4.7 km, respectively. For both of these sections, the distribution of negative phase depths observed (Figure 17) shows considerable complexity. Beneath the Payette Section, negative phase depths vary from roughly 40 km to 90 km, with considerable populations centered at roughly 45 km, 60 km, 75 km and 85 km. Similar variations and multimodal clustering are observed beneath the Snake River Plain. Hopper et al. (2014) observed negative phase depths beneath the Snake River Plain to vary from roughly 50 km to roughly 90 km, in agreement with our results.

Discussion

Negative Phase Interpretation

Until now we have been careful not to make any assumptions about what the negative phases we have identified in the results section represent in terms of seismic structure. There is significant variation in the depths at which the depth of the LAB is found globally, depending on the type of lithosphere (e.g., oceanic versus continental, rifting versus cratonic, etc.; Fischer et al., 2010; Fischer et al., 2020). In tectonically active regions the

LAB is commonly found to be as shallow as 50-70 km (Yuan et al., 2011), but in more stable, cratonic regions, the LAB is typically observed at depths greater than 150 km and has been inferred to be deeper than 200 km in some regions (e.g., Humphreys et al., 2015). In this study, we assume the selected negative phase discussed above in our results is the LAB. This assumption is based on good agreement between LAB depths constrained in previously published receiver function studies of this region (Abt et al., 2010; Ford et al., 2014; Lekic et al., 2011; Levander & Miller, 2012; Li et al., 2007) and estimates of lithospheric thickness inferred from tomographic models (Rau & Forsyth, 2011; Schmandt & Humphreys, 2010). While this assumption is reasonable, the presence of multiple negative phases in some regions of our study (i.e., cross section I-I'; Figure 10) suggests that our approach of selecting only the largest/first negative phase may not be adequate in all instances.

The importance of carefully interpreting seismic structure from receiver functions is evidenced by the work of Rychert and Shearer (2009). Rychert and Shearer (2009) used Ps receiver functions to characterize mantle structure and made a similar assumption regarding phase picks to ours, and argued for a negative phase corresponding with the LAB at depths of 70 to 95 km globally, including beneath the cratons, in disagreement with most, if not all, tomography estimates. Beneath cratonic South Africa they estimated LAB depths of 100 km, while constraints from surface waves put estimates of lithospheric thickness at 200 km (Fishwick, 2010), a significant disagreement. Fishwick (2010) concluded their study cautioning against automatically associating a discontinuity from fast to slow

velocities as indicating the lithosphere–asthenosphere boundary. In retrospect, the negative phases observed by Rychert and Shearer (2009) were early evidence for relatively shallow (60–110 km) negative velocity gradients, commonly referred to as Mid-Lithospheric Discontinuities (MLDs; e.g., Fischer et al., 2020; Krueger et al., 2021), present within the cratonic lithosphere, the origins of which are still debated (Birkey et al., 2021). In the discussion we consider more carefully the role of tomography in interpreting Sp receiver function results.

The assumption that the negative phase we characterize is the LAB has implications for the interpretation of our results. Similar to the work of Levander and Miller (2012), we observe that the LAB often experiences abrupt lateral changes in depth, as can be seen in both Figure 9 (i.e., cross section A-A', 123°W, 120°W–118°W) and Figure 10 (i.e., cross section J-J', 38°N–37°N, 35°N–33°N), and in the map view of Figure 11. These sharp transitions are smoothed in the plot obtained by the automated phase picking algorithm, due to the effects of a Gaussian filter (Figure 12). In some instances, the steep variations in depth appear to be related to regions where more than one negative phase is observed. We see doubling of the negative phase most clearly in cross sections B-B', F-F', and I-I' (Figures 9 & 10). The doubled negative phase in section I-I' has picked LAB depths that alternate between the upper and lower layers of the doubling as a result of the process previously described for picking a single negative phase, resulting in sharp jumps in LAB depth between ~40 km and ~80 km under the Inner Borderlands. Previous studies have found locations in which multiple negative phases occur at two depths within 50 km of

each other vertically, causing the pick of the LAB to jump (i.e., Ford et al., 2014; Hopper & Fischer, 2018; Lekic et al., 2011). Duplexing of a negative phase may be the result of steep lateral changes in depth of the LAB, as evidenced by two-dimensional receiver function modeling (Lekic & Fischer, 2017). However, instances of abrupt lithospheric thinning combined with certain ray path orientations (i.e., the thinning of the lithosphere near the Salton Trough), may be well enough resolved to be devoid of duplexing (Lekic & Fischer, 2017). Critically, the effects of rapidly varying three-dimensional structure on receiver functions has not yet been systematically explored and future work will focus on interrogating such relationships in hopes of improving both our imaging techniques as well as our interpretive framework.

Physiographic Dependence of the LAB

In this study we have used physiographic provinces and sections to help frame the description of our results. Similar to other studies (Hopper & Fischer, 2018; Liu & Gao, 2018; Schmandt & Humphreys, 2010), we treat the physiographic regions as proxies for tectonically or geologically distinct regions. It is important to note that while many studies use modifications of the physiographic provinces shown in this study, they do not all use the same boundaries. For example, physiographic provinces such as the Basin and Range, Columbia Plateau, and Colorado Plateau are commonly used identifiers (e.g., Hopper & Fischer, 2018; Levander et al., 2011; Schmandt & Humphreys, 2010), but it appears less common to group the Pacific Border or the Cascade-Sierra Mountains into singular sections as Fenneman (1931) does.

A key question that this study aims to address is to what extent the surface expression of tectonic activity, quantified in this case using physiographic provinces and sections, is related to the properties (depth, velocity gradient) of the lithosphere-asthenosphere boundary. As a general observation, we find that changes in the depth or amplitude of the LAB phase do not correspond to regional tectonic variation – this finding is in agreement with the qualitative assessment of Hopper and Fischer (2018). Although a handful of exceptions exist; at the boundaries, or nearing the boundaries, some physiographic sections experience changes of LAB depth. This change in LAB depth is clearly seen at the boundary between the High Plateaus of Utah and Grand Canyon Sections of the Colorado Plateau Province in the cross-section K-K' (Figure 10), and was also seen in the map of LAB values produced by Lekic and Fischer (2014). A significant increase in the depth of the LAB is seen at the boundary between the Klamath Mountains and Middle Cascade Mountains in cross-section A-A' (Figure 9), in agreement with observations from Liu and Gao (2018).

Within provinces, some sections appear to have more consistent LAB depths and amplitude while others display a greater range. The Sierra Nevada Section (Cascade-Sierra Province) and Great Basin Section (Basin & Range Province) have the smallest bootstrapped depth ranges_B (Table 1) although the distribution of depths within each section varies considerably. The Sierra Nevada Section has a majority of its depth picks concentrated within 20 km and centered around 65.3 km. The consistency of the LAB depth in this

section, as displayed in red in cross-sections H-H' and I-I' (Figure 10), suggests that this section is acting as a uniform block, as discussed by Stevens et al. (2013). The Great Basin Section has the widest range of LAB depths of any section, however depths are centered around the average of 66.6 km and the calculated depth range_B is less than 2 km. The Great Basin has potential duplexing features in cross sections A-A' (122°W-121°W) and B-B' (118°W-117°W, 115°W-114°W), but otherwise presents as a singular, vertically broad negative phase (Figure 9). Another section with relatively consistent LAB features is the Los Angeles Ranges. Although the Los Angeles Ranges Section contains the Inner Borderlands, which is represented by the grouping of picks for the LAB surrounding 40 km in the histogram for the section, depths are otherwise tightly centered around an average of 67.7 km (Figure 13). The Inner Borderlands are a well constrained region of thinned lithosphere, previously observed by Ford et al. (2014) and Lekic et al. (2011) and are thought to be the result of the extension due to the rotation of the Transverse Ranges approximately 20 million years ago (Nicholson et al., 1994). Another section where the effects of tectonic processes are thought to be demonstrated in the distribution of LAB depth picks is the Salton Trough. The Salton Trough has a bimodal distribution of depth picks, with one grouping shallower than 50 km and the other deeper than 60 km (Figure 15). The shallower set of depths in this region is believed to be the result of transtensional motion associated with strike-slip motion of the San Andreas Fault System and seafloor spreading in the Gulf of California (Lekic et al., 2011).

Volcanic Controls on the LAB

The velocity decrease defining the transition from lithosphere to asthenosphere can be driven by things such as changes in mantle temperature, volatile content, bulk composition including mineralogy, the presence of partial melt, mantle mineral grain size, and the presence (or not) of anisotropic fabrics in the mantle rock, which are themselves impacted by tectonic and magmatic processes (e.g., Hopper et al., 2014). Each of these factors has an individual impact on seismic velocities, however, variations in volatile (e.g., water) and melt content are required to create the sharp velocity changes seen in receiver functions in some regions, such as eastern Australia (Ford et al., 2010). Likewise, in the eastern U.S., a strong, sharp transition between the lithosphere and asthenosphere is most easily explained by the presence of a small amount of melt in the asthenosphere (Rychert et al., 2005). In areas with more recent volcanic history (e.g., High Lava Plains), a lack of large negative phases has been used to support the presence of melt in both the lithosphere and asthenosphere (Hopper et al., 2014). The presence of partial melt can also be inferred from tomographic models. Schmandt and Humphreys (2010) found a strong correlation between the location of young volcanic fields and low seismic velocities in the asthenosphere in the western U.S. A thin lithosphere in the western U.S., likely to be underlain by partial melt, was also inferred from anelasticity models and basalt thermobarometry (Porter & Reid, 2021). The surface wave tomography model produced by Rau and Forsyth (2011) uses the presence of melt to explain shear velocities in the mantle lower than 4.2 km/s.

The Walker Lane region of eastern California has been impacted by numerous volcanic events within the last 15 Ma and has thus been the focus of several of the petrologic studies in the region (Gazel et al. 2012; Putirka & Platt, 2012; Putirka et al., 2012). Plank and Forsyth (2016) found the petrologic LAB to be at a depth of 66 km beneath the Big Pine Volcanic Field, based on a joint petrologic and seismic approach, which agrees well with the 62.6 km LAB phase observed in this study (Figure 18). Putirka et al. (2012) found the chemical mantle lithosphere at Coso Volcanic Field to be close to completely degraded, inferred to be the result of extension and resulting lithospheric thinning. However, we observe the LAB depth to be 76.8 km, roughly 10 km deeper than the regional average (Figure 18). Rau and Forsyth (2011) found anomalously slow velocities directly beneath Coso at depths of 60-70 km, which better aligns with the preferred interpretation of Putirka et al. (2012).

Due to the recent history of active tectonics and volcanism in the western US, we performed a preliminary analysis to determine differences in the depth of the LAB phase surrounding three volcanic centers, which we compare to a control region (Figure 19). The control region is centered at 41°N, 114°W, just east of the Nevada-Utah border, and was chosen due to its lack of recent surface volcanism. The three volcanic centers chosen are Lassen Volcanic Center (40.5°N, 121.5°W), Mammoth Mountain (37.2°N, 119°W), and Salton Buttes (33.2°N, 115.6°W). Due to the way in which the negative phase depth values were discretized, values for the negative phase only exist at every 0.1° in latitude and longitude. Therefore, we created boxes of four different half-widths centered on each of these points

(0.1° , 0.25° , 0.5° , 0.75°) to better understand how LAB properties change as a function of distance away from a given volcanic center.

The average depth of the negative phase for each of these centers changes with changing half-width as increasingly larger areas are averaged. Each of the four centers are shown in (Figure 19) and the averages are listed in (Table 3). The average depth of the negative phase increases with increasing half-width for the control region and decreases with increasing half-width for Mammoth Mountain and Salton Buttes. Lassen Volcanic Center experiences fluctuations in the average depth of the negative phase as the distance from the volcanic center increases. At the largest half-width of 0.75° around each site, the control region has an average negative phase that is ~ 10 km deeper than Mammoth Mountain and ~ 20 km deeper than both Lassen Volcanic Center and Salton Buttes.

The average depth of the LAB was calculated for each box size at each location, and the averages were bootstrapped over, as was described for the physiographic provinces. These values are presented in Table 3. The largest variation between the unbootstapped and bootstrapped LAB depth values is 0.2 km for a half-width of 0.5° around Salton Buttes. The bootstrapping process better constrains the depth range of the LAB for half-width boxes larger than 0.1° at all locations. The bootstrapping process likely did not affect the depth range of the negative phase for most places at a half-width of 0.1° because this distance only had 4 depth points from which the bootstrapping could be performed. The

bootstrapping process most impacted the expected depth range of the LAB for the half-width of 0.75° , by reducing each to ~10% of its original.

The effects of the bootstrapping process are displayed in Figure 20. Histograms of the depth distribution were generated for half-widths of 0.5° and 0.75° since they had a maximum 100 and 225 depth points possible, respectively. These histograms show the same information as the histograms for each of the physiographic provinces (i.e., depth range of non-bootstrapped and bootstrapped values, average depth of LAB, confidence interval for the bootstrapping process). The control region has a non-uniform distribution of depths for both half-widths before bootstrapping, with the 0.75° half-width having a bimodal distribution around the average, but both half-widths converge to a unimodal distribution centered to the right of the average LAB depth after bootstrapping. Lassen Volcanic Center has a normal distribution of depths before and after bootstrapping for both half-widths, however, the width of the distribution narrows after bootstrapping to within 3 km for a 0.75° half-width and within 2 km for a 0.5° half-width. Mammoth Mountain has bimodal distributions with a larger grouping at deeper depths before bootstrapping that, after bootstrapping, converges to a unimodal distribution for both half-widths. The Salton Buttes have the clearest bimodal distribution before bootstrapping, with more than 10 km in depth separating the two modes at 0.5° and ~10 km separating the modes at 0.75° . Both Salton Buttes depth distributions become unimodal after bootstrapping, but this volcanic center has the largest remaining depth range.

Tomography as a Constraint on the LAB

Comparison of receiver functions to tomography can be a crucial step when trying to identify the lithosphere-asthenosphere boundary in receiver functions (e.g., Abt et al., 2010; Birkey et al., 2021; Hopper et al., 2014). Tomography models are generated using different combinations of data including surface waves (Debayle & Kennett, 2000; Li & Burke, 2006) or body waves (Frederiksen et al., 2001; Schmandt & Humphreys, 2011), a combination of both (Bedle et al., 2021; Golos et al., 2018), and sometimes include other observables (Li et al., 2003; Simmons et al., 2010). Some tomography models report seismic wave speed values as a percent anomaly relative to a reference model (Porritt et al., 2014; Schmandt & Lin, 2014) while others report values in terms of absolute velocity (e.g., Porter et al., 2015; Shen & Ritzwoller, 2016). Tomographic models can be used to identify variations in the lithosphere-asthenosphere system by looking for changes in the high velocity lithospheric lid relative to the lower velocity asthenosphere (Fischer et al., 2010). A common method for constraining the depth of the LAB from tomographic models is the by finding the depth range of the largest negative velocity gradient, or by locating the depth to the center of the negative gradient below the high-velocity lid (Debayle & Kennett, 2000; Li et al., 2003; Weeraratne et al., 2003). Other methods include using a specified percent velocity variation relative to a global reference model (e.g., Frederiksen et al., 2001; Simons & van der Hilst, 2002), using a specified absolute velocity variation with depth (e.g., Li & Burke, 2006), and decreases in lateral velocity changes associated with the transition from the lithosphere to the asthenosphere (Bruneton et al., 2004). Porter and Reid (2021) determined thermal LAB depth by combining a shear-wave velocity

model with empirically derived anelasticity models for temperature. It should be noted that seismic proxies for determining the location of the LAB are not limited to isotropic velocity changes. Gaherty and Jordan (1995) used changes in the magnitude of seismic anisotropy to determine the location of the LAB. Combining anisotropy measurements and velocity changes, Yuan et al. (2011) generated a 3-D shear velocity model and use the model to determine the depth of the LAB.

A compelling example of the utility of comparing receiver functions to tomography models comes from the study of the lithospheric mantle beneath cratons. In Australia, tomography models indicate lithosphere as thick as 250 km beneath its cratons, while early receiver function studies of the cratons interpreted negative phases as the LAB shallower than 100 km (Kumar et al., 2007; Rychert & Shearer, 2009). Ford et al. (2010) compared the depth of the largest statistically significant negative phase at each station (similar to our approach) to the expected depth of the LAB, defined as the range between the minimum S-wave velocity beneath the Moho and the first velocity maximum above it, using the velocity model of Fishwick et al. (2008), which they called “the potential LAB depth range”. The study found that the dominating negative phase is not always located within this potential LAB depth range, but rather above it, and were therefore termed mid-lithospheric discontinuities (MLDs).

Although our study area is not expected to have thick, cratonic lithosphere, the comparison of tomography models to better understand our results is essential, particularly in the

context of better understanding the structure of the seismic lithosphere and asthenosphere. Global (e.g., Schaeffer & Lebedev, 2013) and regional (e.g., Schmandt & Humphreys, 2010; Shen & Ritzwoller, 2016) tomographic models consistently find relatively shallow (~60-80 km) lithospheric thickness in the western U.S., although there are some exceptions to this. The Transverse Ranges appear to be underlain by thicker lithosphere (Rau & Forsyth, 2011; Schmandt & Humphreys, 2010), while the Mojave has a thinner lithosphere (Shen & Ritzwoller, 2016), including beneath the Eastern California Shear Zone (Rau & Forsyth, 2011). Although we do not see a thicker lithosphere beneath most of the Transverse Ranges, we do image a generally thinner than average lithosphere in the Eastern California Shear Zone. Another distinctive feature of tomography models in the region is the appearance of a fast seismic velocity feature beneath the southern Great Valley in California, commonly referred to as the Isabella Anomaly (Rau & Forsyth, 2011; Schmandt & Humphreys, 2010). The Isabella Anomaly has alternatively been described as a remnant microplate (Wang et al., 2013), while other interpretations include lithospheric foundering (Zandt et al., 2004).

The next step in our analysis is to better understand the implications of the picks made as they compare to tomography models. We have completed a preliminary analysis with the model generated by Shen and Ritzwoller (2016). The model is an absolute Vs model covering the contiguous United States down to a depth of 150 km and relies on the joint inversion of surface waves (ambient noise and earthquake) and Ps receiver functions (for constraining crustal structure). We chose this model as surface wave models are more

sensitive to variations in velocity with depth, relative to body waves, and are therefore better at identifying transitions from lithosphere to asthenosphere. While the model extends to a depth of only 150 km, making it unsuitable for identifying the LAB in cratonic regions, the average LAB depth in the western U.S. is shallow enough to be imaged by their methodology. Meanwhile, the inclusion of ambient noise and Ps receiver functions ensures that the uppermost mantle is well constrained. Using the absolute shear velocities from this model, downloaded from IRIS Earth Model Collaboration (EMC), we first searched for the location of the maximum negative velocity gradient along one-dimensional velocity profiles at each point in latitude-longitude space within our study area. Using the maximum negative velocity gradient, we then searched above it and below it to determine the maximum and minimum of the velocities along the same profile. Similar to others (Abt et al., 2010; Birkey et al., 2021; Ford et al., 2010; Goldhagen et al., in press), we assume the maximum velocity corresponds to an arbitrary point within the lithosphere and the minimum velocity corresponds to an arbitrary point within the asthenosphere. Therefore, the transition from the maximum velocity to minimum velocity is thought to represent the entire depth range over which the transition from lithosphere to asthenosphere can potentially occur.

Examples of three one-dimensional profiles from the Shen and Ritzwoller (2016) model are shown in Figure 21. In two of the profiles (cyan, magenta), we mark the depths of the minimum and maximum velocities, along with the maximum negative velocity gradient. In the case of the cyan profile, the maximum velocity occurs directly beneath the Moho

(rapid increase in velocity at 31 km), immediately followed by the maximum negative velocity gradient. The minimum velocity is observed at 61 km depth. We characterize this profile as having a very rapid and shallow lithosphere to asthenosphere transition. Beneath the magenta profile we observe a positive velocity gradient beneath the Moho that extends to a depth of 104 km (maximum velocity depth) followed by a negative velocity gradient to 147.5 km depth (minimum velocity depth). The maximum negative velocity gradient is observed at a depth approximately midway between the maximum and minimum velocities. The magenta profile exhibits a more gradual lithosphere to asthenosphere transition that begins at a greater depth. The third profile (dashed black line) is an example of a profile in which we do not select a minimum or maximum velocity, as no negative velocity gradient exists. It is possible that a negative velocity gradient exists below the depth of the tomography model, or that a negative velocity gradient exists in the Earth over a limited depth extent within the depth range interrogated by the surface waves but is not imaged because of the limited vertical resolution of surface waves. Another possibility is that active dynamic processes may be obscuring the lithosphere-asthenosphere boundary. The dash black profile sits within the boundaries of the Isabelle Anomaly, a region of fast velocities potentially associated with downwelling lithosphere (Zandt et al., 2004).

We compared characteristics of the LAB determined from the tomography model of Shen and Ritzwoller (2016) to characteristics of our LAB picks from receiver functions (e.g., depth, amplitude) to better understand how these methodologies may be used together to better constrain the seismic properties of the LAB. To begin, we compare the LAB depth

(from receiver functions) to the depth of the minimum and maximum velocities, and the depth of the maximum negative velocity gradient (top row, Figure 22). While no clear one-to-one correlation exists between the inferred LAB depths from receiver functions and any of the three computed variables from the tomography model, we do make one important observation, which is that the majority of the LAB depths determined from receiver functions fall within our tomographically inferred lithosphere (maximum velocity) to asthenosphere (minimum velocity) transition. In total, 91% of the receiver function picks are observed at a depth below the maximum velocity and 83% of the receiver function picks are observed at a depth above the minimum velocity. This observation confirms our early assertion that tomography models and receiver functions broadly agree. However, the lack of any sort of direct correlation suggests that the two methods diverge considerably in detail. We also note that the majority (78%) of the time, the receiver function inferred LAB depth occurs at a greater depth than the tomographically determined maximum negative velocity gradient. However, this observation is currently of limited value as the gradient was determined in 0.5 km increments, which is beyond the resolution of either surface waves used in the study or Sp receiver functions. Future work will focus on developing a more robust way of constraining the maximum negative velocity gradient.

The amplitude of the LAB phase from receiver functions is a function of velocity gradient, and therefore is sensitive to both the thickness of the velocity gradient, as well as the velocity contrast across the boundary (Rychert et al., 2007). We compare LAB amplitude (from receiver functions) to the depths of the minimum velocity, maximum velocity, and

maximum negative velocity gradient from the Shen and Ritzwoller (2016) model, but find little agreement (middle row, Figure 22). We then compare the receiver function computed amplitudes to the calculated gradient thickness, velocity contrast, and total inferred gradient (gradient thickness/velocity contrast) from tomography, assuming the gradient begins and ends at the maximum and minimum velocities determined from tomography. Since tomography models have more limited vertical resolution than receiver functions, and because tomography models are typically damped, the tomographically inferred estimates are likely to overestimate the gradient thickness and underestimate the total percent velocity contrast present in the Earth. Again, we see little evidence of a direct correlation, although the plot of LAB amplitude versus velocity contrast (bottom middle, Figure 22) exhibits a weak trend in which a larger velocity contrast equals a larger amplitude LAB phase from receiver functions. In Figure 23 we explore this relationship more carefully by plotting the LAB phase amplitude against the maximum and minimum velocities (km/s) and find that a weak but negative correlation exists between the minimum velocity and receiver function amplitude. The trend between smaller amplitude phases and larger minimum velocities would be expected in regions where slower-than-average asthenosphere underlying average velocity lithosphere would generate a more pronounced (i.e., larger amplitude) LAB phase in receiver functions.

Conclusions

In this study we generated CCP stacked Sp receiver functions for the southwestern U.S., from the western coast of California to the eastern edge of the Basin and Range. We

interpret the largest observed negative phase to be the lithosphere-asthenosphere boundary based on qualitative comparisons to previous studies including tomography and receiver function analysis. The LAB depth picks were compared to physiographic provinces and sections, selected regions of volcanism, and the tomography model of Shen and Ritzwoller (2016) in order to determine to what extent, if any, relation exists between them. The underlying assumption that we make in comparing receiver function LAB depths to physiographic provinces is that the provinces represent the manifestation of tectonics at the Earth's surface. Another assumption embedded in this approach is that tectonic activity will manifest itself in changes to the nature of the seismic lithosphere. While continental scale correlations between thermotectonic age and lithospheric thickness exist (Porter et al., 2019), it is unclear if these correlations hold at the scale imageable by receiver functions. In our analysis we observe a handful of places in which variations in LAB depth appear to be related to a given physiographic province or section, but for the majority of the study area we find little correlation. In some instances, highly localized changes within a physiographic boundary (i.e., Inner Borderlands, Salton Trough) are observed and potentially highlighted due to the use of the province or section boundaries. We conclude that utilizing physiographic provinces as proxies for tectonic terranes is useful in establishing a framework with which to compare results across studies, but we find little evidence to suggest that these provinces and sections have seismic structure that is uniquely related to their surface manifestation. In the preliminary analysis of the potential effects of volcanism on lithospheric structure, we find that our results do not always agree with petrologic estimates of LAB depth, and the results can diverge significantly. For the case

study of volcanic centers compared to the control location, we find that the volcanic centers have shallower LAB depths than the control location and LAB depth varies for all locations away from the center.

The integration of Sp receiver functions and tomographic models is an emerging topic of exploration in the seismic community. However, before we can successfully integrate the two methods we need to understand the extent to which they agree, particularly as tomography models are used to determine with receiver function phases are MLDs or LABs (e.g., Birkey et al., 2021). When compared to the tomography model of Shen and Ritzwoller (2016), there is generally good agreement for the depth of the LAB as determined by receiver functions, with 91% of inferred LAB phases falling below the maximum velocity (inferred upper limit of the potential LAB). However, a simple one-to-one correlation does not exist, due in large part to the different sensitivities of each method. A weak correlation between LAB amplitude and velocity contrast is observed, which is likely controlled by the negative correlation between LAB amplitude and minimum velocity, suggesting the LAB amplitudes in receiver functions are influenced by the velocities in the asthenosphere rather than the lithosphere. This runs counter to the conclusions of Ford et al. (2014) which argued that the change in amplitude across the Pacific-North American Plate Boundary is controlled by differences in lithospheric structure, however, more work is needed to understand the disparity in results.

References

- Abt, D. L., Fischer, K. M., French, S. W., Ford, H. A., Yuan, H., & Romanowicz, B. (2010). North American lithospheric discontinuity structure imaged by Ps and Sp receiver functions. *Journal of Geophysical Research: Solid Earth*, 115(B9).
- Ainsworth, R., Pulliam, J., Gurrola, H., & Evanzia, D. (2014). Sp receiver function imaging of a passive margin: Transect across Texas's Gulf Coastal Plain. *Earth and Planetary Science Letters*, 402, 138-147.
- Artemieva, I. (2011). *Lithosphere: an interdisciplinary approach*. Cambridge University Press.
- Atwater, T. (1970). Implications of plate tectonics for the Cenozoic tectonic evolution of western North America. *Geological Society of America Bulletin*, 81(12), 3513-3536.
- Atwater, T. (1989). Plate tectonic history of the northeast Pacific and western North America.
- Atwater, T., & Stock, J. (1998). Pacific-North America plate tectonics of the Neogene southwestern United States: an update. *International Geology Review*, 40(5), 375-402.
- Ba, K., Gao, S. S., Liu, K. H., Kong, F., & Song, J. (2020). Receiver function imaging of the 410 and 660 km discontinuities beneath the Australian continent. *Geophysical Journal International*, 220(3), 1481-1490.
- Bedle, H., Lou, X., & Van der Lee, S. (2021). Continental Tectonics Inferred From High-Resolution Imaging of the Mantle Beneath the United States, Through the Combination of USArray Data Types. *Geochemistry, Geophysics, Geosystems*, 22(10), e2021GC009674.
- Beeler, N. M., Lockner, D. L., & Hickman, S. H. (2001). A simple stick-slip and creep-slip model for repeating earthquakes and its implication for microearthquakes at Parkfield. *Bulletin of the Seismological Society of America*, 91(6), 1797-1804.
- Birkey, A., Ford, H. A., Dabney, P., & Goldhagen, G. (2021). The lithospheric architecture of Australia from seismic receiver functions. *Journal of Geophysical Research: Solid Earth*, 126(4), e2020JB020999.
- Bostock, M. G. (1998). Mantle stratigraphy and evolution of the Slave province. *Journal of Geophysical Research: Solid Earth*, 103(B9), 21183-21200.

- Bruneton, M., Pedersen, H. A., Farra, V., Arndt, N. T., Vacher, P., Achauer, U., ... & Yurov, Y. G. (2004). Complex lithospheric structure under the central Baltic Shield from surface wave tomography. *Journal of Geophysical Research: Solid Earth*, 109(B10).
- Camp, V. E., Pierce, K. L., & Morgan, L. A. (2015). Yellowstone plume trigger for Basin and Range extension, and coeval emplacement of the Nevada–Columbia Basin magmatic belt. *Geosphere*, 11(2), 203-225.
- Crotwell, H. P., Owens, T. J., & Ritsema, J. (1999). The TauP Toolkit: Flexible seismic travel-time and ray-path utilities. *Seismological Research Letters*, 70, 154-160.
- Debayle, E., & Kennett, B. L. N. (2000). Anisotropy in the Australasian upper mantle from Love and Rayleigh waveform inversion. *Earth and Planetary Science Letters*, 184(1), 339-351.
- Eaton, D. W., Darbyshire, F., Evans, R. L., Grütter, H., Jones, A. G., & Yuan, X. (2009). The elusive lithosphere–asthenosphere boundary (LAB) beneath cratons. *Lithos*, 109(1-2), 1-22.
- Faulds, J. E., Henry, C. D. (2008). Tectonic influences on the spatial and temporal evolution of the Walker Lane: An incipient transform fault along the evolving Pacific–North American plate boundary. Ores and orogenesis: Circum-Pacific tectonics, geologic evolution, and ore deposits: *Arizona Geological Society Digest*, 22, 437-470.
- Fenneman, N.M. (1931). *Physiography of Western United States*. 1st ed. McGraw-Hill book company, inc.
- Fenneman, N.M., Johnson, D.W. (1946). *Physiographic divisions of the coterminous U.S.*
- Feuerbach, D. L., Smith, E. I., Walker, J. D., & Tangeman, J. A. (1993). The role of the mantle during crustal extension: Constraints from geochemistry of volcanic rocks in the Lake Mead area, Nevada and Arizona. *Geological Society of America Bulletin*, 105(12), 1561-1575.
- Fischer, K. M., Ford, H. A., Abt, D. L., & Rychert, C. A. (2010). The lithosphere–asthenosphere boundary. *Annual Review of Earth and Planetary Sciences*, 38, 551-575.
- Fischer, K. M., Rychert, C. A., Dalton, C. A., Miller, M. S., Beghein, C., & Schutt, D. L. (2020). A comparison of oceanic and continental mantle lithosphere. *Physics of the Earth and Planetary Interiors*, 309, 106600.

- Fishwick, S., Heintz, M., Kennett, B. L. N., Reading, A. M., & Yoshizawa, K. (2008). Steps in lithospheric thickness within eastern Australia, evidence from surface wave tomography. *Tectonics*, 27(4).
- Fishwick, S. (2010). Surface wave tomography: imaging of the lithosphere–asthenosphere boundary beneath central and southern Africa?. *Lithos*, 120(1-2), 63-73.
- Ford, H. A., Fischer, K. M., Abt, D. L., Rychert, C. A., & Elkins-Tanton, L. T. (2010). The lithosphere–asthenosphere boundary and cratonic lithospheric layering beneath Australia from Sp wave imaging. *Earth and Planetary Science Letters*, 300(3-4), 299-310.
- Ford, H. A., Fischer, K. M., & Lekic, V. (2014). Localized shear in the deep lithosphere beneath the San Andreas fault system. *Geology*, 42(4), 295-298.
- Forsyth, D. W. (1975). The early structural evolution and anisotropy of the oceanic upper mantle. *Geophysical Journal International*, 43(1), 103-162.
- Frederiksen, A. W., Bostock, M. G., & Cassidy, J. F. (2001). S-wave velocity structure of the Canadian upper mantle. *Physics of the Earth and Planetary Interiors*, 124(3-4), 175-191.
- Frassetto, A. M., Zandt, G., Gilbert, H., Owens, T. J., & Jones, C. H. (2011). Structure of the Sierra Nevada from receiver functions and implications for lithospheric foundering. *Geosphere*, 7(4), 898-921.
- Gaherty, J. B., & Jordan, T. H. (1995). Lehmann discontinuity as the base of an anisotropic layer beneath continents. *Science*, 268(5216), 1468-1471.
- Gazel, E., Plank, T., Forsyth, D. W., Bendersky, C., Lee, C. T. A., & Hauri, E. H. (2012). Lithosphere versus asthenosphere mantle sources at the Big Pine Volcanic Field, California. *Geochemistry, Geophysics, Geosystems*, 13(6).
- Goldhagen, G., Ford, H.A., & Long, M.D. (in press). Evidence for a lithospheric step and pervasive lithospheric thinning beneath southern New England, northeastern USA. *Geology*.
- Golos, E. M., Fang, H., Yao, H., Zhang, H., Burdick, S., Vernon, F., ... & Van der Hilst, R. D. (2018). Shear wave tomography beneath the United States using a joint inversion of surface and body waves. *Journal of Geophysical Research: Solid Earth*, 123(6), 5169-5189.

- Griffin, W. L., O'Reilly, S. Y., Doyle, B. J., Pearson, N. J., Coopersmith, H., Kivi, K., Malkovets, V. and Pokhilenko, N. (2004). Lithosphere mapping beneath the North American plate. *Lithos*, 77(1-4), 873-922.
- Helfrich, G. (2006). Extended-time multitaper frequency domain cross-correlation receiver-function estimation. *Bulletin of the Seismological Society of America*, 96(1), 344-347.
- Hopper, E., Ford, H. A., Fischer, K. M., Lekic, V., & Fouch, M. J. (2014). The lithosphere–asthenosphere boundary and the tectonic and magmatic history of the northwestern United States. *Earth and Planetary Science Letters*, 402, 69-81.
- Hopper, E., & Fischer, K. M. (2018). The changing face of the lithosphere-asthenosphere boundary: Imaging continental scale patterns in upper mantle structure across the contiguous US with Sp converted waves. *Geochemistry, Geophysics, Geosystems*, 19(8), 2593-2614.
- Kennett, B. L., Engdahl, E. R., & Buland, R. (1995). Constraints on seismic velocities in the Earth from traveltimes. *Geophysical Journal International*, 122(1), 108-124.
- Kind, R., Yuan, X., & Kumar, P. (2012). Seismic receiver functions and the lithosphere–asthenosphere boundary. *Tectonophysics*, 536, 25-43.
- Krueger, H. E., Gama, I., & Fischer, K. M. (2021). Global Patterns in Cratonic Mid-Lithospheric Discontinuities From Sp Receiver Functions. *Geochemistry, Geophysics, Geosystems*, 22(6), e2021GC009819.
- Kumar, P., Yuan, X., Kumar, M. R., Kind, R., Li, X., & Chadha, R. K. (2007). The rapid drift of the Indian tectonic plate. *Nature*, 449(7164), 894-897.
- Lavayssière, A., Rychert, C., Harmon, N., Keir, D., Hammond, J. O., Kendall, J. M., ... & Leroy, S. (2018). Imaging lithospheric discontinuities beneath the Northern East African Rift using S-to-P receiver functions. *Geochemistry, Geophysics, Geosystems*, 19(10), 4048-4062.
- Lee, C. T. A. (2003). Compositional variation of density and seismic velocities in natural peridotites at STP conditions: Implications for seismic imaging of compositional heterogeneities in the upper mantle. *Journal of Geophysical Research: Solid Earth*, 108(B9).
- Lee, C. T. A., Luffi, P., Plank, T., Dalton, H., & Leeman, W. P. (2009). Constraints on the depths and temperatures of basaltic magma generation on Earth and other terrestrial planets using new thermobarometers for mafic magmas. *Earth and Planetary Science Letters*, 279(1-2), 20-33.

- Lekic, V., French, S. W., & Fischer, K. M. (2011). Lithospheric thinning beneath rifted regions of Southern California. *Science*, 334(6057), 783-787.
- Lekić, V., & Fischer, K. M. (2014). Contrasting lithospheric signatures across the western United States revealed by Sp receiver functions. *Earth and Planetary Science Letters*, 402, 90-98.
- Lekić, V., & Fischer, K. M. (2017). Interpreting spatially stacked Sp receiver functions. *Geophysical Journal International*, 210(2), 874-886.
- Levander, A., Schmandt, B., Miller, M. S., Liu, K., Karlstrom, K. E., Crow, R. S., ... & Humphreys, E. D. (2011). Continuing Colorado plateau uplift by delamination-style convective lithospheric downwelling. *Nature*, 472(7344), 461-465.
- Levander, A., & Miller, M. S. (2012). Evolutionary aspects of lithosphere discontinuity structure in the western US. *Geochemistry, Geophysics, Geosystems*, 13(7).
- Li, A., Forsyth, D. W., & Fischer, K. M. (2003). Shear velocity structure and azimuthal anisotropy beneath eastern North America from Rayleigh wave inversion. *Journal of Geophysical Research: Solid Earth*, 108(B8).
- Li, A., & Burke, K. (2006). Upper mantle structure of southern Africa from Rayleigh wave tomography. *Journal of Geophysical Research: Solid Earth*, 111(B10).
- Li, X., Yuan, X., & Kind, R. (2007). The lithosphere-asthenosphere boundary beneath the western United States. *Geophysical Journal International*, 170(2), 700-710.
- Liu, L., & Gao, S. S. (2018). Lithospheric layering beneath the contiguous United States constrained by S-to-P receiver functions. *Earth and Planetary Science Letters*, 495, 79-86.
- Liu, T., & Shearer, P. M. (2021). Complicated Lithospheric Structure Beneath the Contiguous US Revealed by Teleseismic S-Reflections. *Journal of Geophysical Research: Solid Earth*, 126(5), e2020JB021624.
- Nettles, M., & Dziewoński, A. M. (2008). Radially anisotropic shear velocity structure of the upper mantle globally and beneath North America. *Journal of Geophysical Research: Solid Earth*, 113(B2).
- Nicholson, C., Sorlien, C. C., Atwater, T., Crowell, J. C., & Luyendyk, B. P. (1994). Microplate capture, rotation of the western Transverse Ranges, and initiation of the San Andreas transform as a low-angle fault system. *Geology*, 22(6), 491-495.

- Nishimura, C. E., & Forsyth, D. W. (1989). The anisotropic structure of the upper mantle in the Pacific. *Geophysical Journal International*, 96(2), 203-229.
- Oskin, M., Stock, J., & Martín-Barajas, A. (2001). Rapid localization of Pacific–North America plate motion in the Gulf of California. *Geology*, 29(5), 459-462.
- Park, J., & Levin, V. (2000). Receiver functions from multiple-taper spectral correlation estimates. *Bulletin of the Seismological Society of America*, 90(6), 1507-1520.
- Plank, T., & Forsyth, D. W. (2016). Thermal structure and melting conditions in the mantle beneath the Basin and Range province from seismology and petrology. *Geochemistry, Geophysics, Geosystems*, 17(4), 1312-1338.
- Porritt, R. W., Allen, R. M., & Pollitz, F. F. (2014). Seismic imaging east of the Rocky Mountains with USArray. *Earth and Planetary Science Letters*, 402, 16-25.
- Porter, R., Liu, Y., & Holt, W. E. (2016). Lithospheric records of orogeny within the continental US. *Geophysical Research Letters*, 43(1), 144-153.
- Porter, R. C., van der Lee, S., & Whitmeyer, S. J. (2019). Synthesizing EarthScope data to constrain the thermal evolution of the continental US lithosphere. *Geosphere*, 15(6), 1722-1737.
- Porter, R., & Reid, M. (2021). Mapping the Thermal Lithosphere and Melting across the Continental US. *Geophysical Research Letters*, 48(7), e2020GL092197.
- Possee, D., Rychert, C., Harmon, N., & Keir, D. (2021). Seismic Discontinuities Across the North American Caribbean Plate Boundary From S-to-P Receiver Functions. *Geochemistry, Geophysics, Geosystems*, 22(7), e2021GC009723.
- Putirka, K., Jean, M., Cousens, B., Sharma, R., Torrez, G., & Carlson, C. (2012). Cenozoic volcanism in the Sierra Nevada and Walker Lane, California, and a new model for lithosphere degradation. *Geosphere*, 8(2), 265-291.
- Putirka, K., & Platt, B. (2012). Basin and Range volcanism as a passive response to extensional tectonics. *Geosphere*, 8(6), 1274-1285.
- Ranalli, G., & Murphy, D. C. (1987). Rheological stratification of the lithosphere. *Tectonophysics*, 132(4), 281-295.
- Rau, C. J., & Forsyth, D. W. (2011). Melt in the mantle beneath the amagmatic zone, southern Nevada. *Geology*, 39(10), 975-978.
- Romanowicz, B. (2009). The thickness of tectonic plates. *Science*, 324(5926), 474-476.

- Rondenay, S. (2009). Upper mantle imaging with array recordings of converted and scattered teleseismic waves. *Surveys in geophysics*, 30(4), 377-405.
- Rychert, C. A., Rondenay, S., & Fischer, K. M. (2007). P-to-S and S-to-P imaging of a sharp lithosphere-asthenosphere boundary beneath eastern North America. *Journal of Geophysical Research: Solid Earth*, 112(B8).
- Rychert, C. A., & Shearer, P. M. (2009). A global view of the lithosphere-asthenosphere boundary. *Science*, 324(5926), 495-498.
- Rychert, C. A., Harmon, N., & Ebinger, C. (2014). Receiver function imaging of lithospheric structure and the onset of melting beneath the Galápagos Archipelago. *Earth and Planetary Science Letters*, 388, 156-165.
- Schaeffer, A. J., & Lebedev, S. (2013). Global shear speed structure of the upper mantle and transition zone. *Geophysical Journal International*, 194(1), 417-449.
- Schmandt, B., & Humphreys, E. (2010). Complex subduction and small-scale convection revealed by body-wave tomography of the western United States upper mantle. *Earth and Planetary Science Letters*, 297(3-4), 435-445.
- Schmandt, B., & Humphreys, E. (2011). Seismically imaged relict slab from the 55 Ma Siletzia accretion to the northwest United States. *Geology*, 39(2), 175-178.
- Schmandt, B., & Lin, F. C. (2014). P and S wave tomography of the mantle beneath the United States. *Geophysical Research Letters*, 41(18), 6342-6349.
- Shen, W., & Ritzwoller, M. H. (2016). Crustal and uppermost mantle structure beneath the United States. *Journal of Geophysical Research: Solid Earth*, 121(6), 4306-4342.
- Simmons, N. A., Forte, A. M., Boschi, L., & Grand, S. P. (2010). GyPSuM: A joint tomographic model of mantle density and seismic wave speeds. *Journal of Geophysical Research: Solid Earth*, 115(B12).
- Simons, F. J., & Van Der Hilst, R. D. (2002). Age-dependent seismic thickness and mechanical strength of the Australian lithosphere. *Geophysical Research Letters*, 29(11), 24-1.
- Sleep, N. H. (2005). Evolution of the continental lithosphere. *Annual Review of Earth and Planetary Sciences*, 33(1), 369-393.

- Stevens, C. H., Stone, P., & Blakely, R. J. (2013). Structural Evolution of the East Sierra Valley System (Owens Valley and Vicinity), California: A Geologic and Geophysical Synthesis. *Geosciences*, 3(2), 176-215.
- Stock, J. M., & Hodges, K. V. (1989). Pre-Pliocene extension around the Gulf of California and the transfer of Baja California to the Pacific plate. *Tectonics*, 8(1), 99-115.
- Wang, Y., Forsyth, D. W., Rau, C. J., Carriero, N., Schmandt, B., Gaherty, J. B., & Savage, B. (2013). Fossil slabs attached to unsubducted fragments of the Farallon plate. *Proceedings of the National Academy of Sciences*, 110(14), 5342-5346.
- Weeraratne, D. S., Forsyth, D. W., Fischer, K. M., & Nyblade, A. A. (2003). Evidence for an upper mantle plume beneath the Tanzanian craton from Rayleigh wave tomography. *Journal of Geophysical Research: Solid Earth*, 108(B9).
- Whitmeyer, S. J., & Karlstrom, K. E. (2007). Tectonic model for the Proterozoic growth of North America. *Geosphere*, 3(4), 220-259.
- Wilson, D. C., Angus, D. A., Ni, J. F., & Grand, S. P. (2006). Constraints on the interpretation of S-to-P receiver functions. *Geophysical Journal International*, 165(3), 969-980.
- Yuan, H., Romanowicz, B., Fischer, K. M., & Abt, D. (2011). 3-D shear wave radially and azimuthally anisotropic velocity model of the North American upper mantle. *Geophysical Journal International*, 184(3), 1237-1260.
- Zandt, G., Gilbert, H., Owens, T. J., Ducea, M., Saleeby, J., & Jones, C. H. (2004). Active foundering of a continental arc root beneath the southern Sierra Nevada in California. *Nature*, 431(7004), 41-46.

Figures

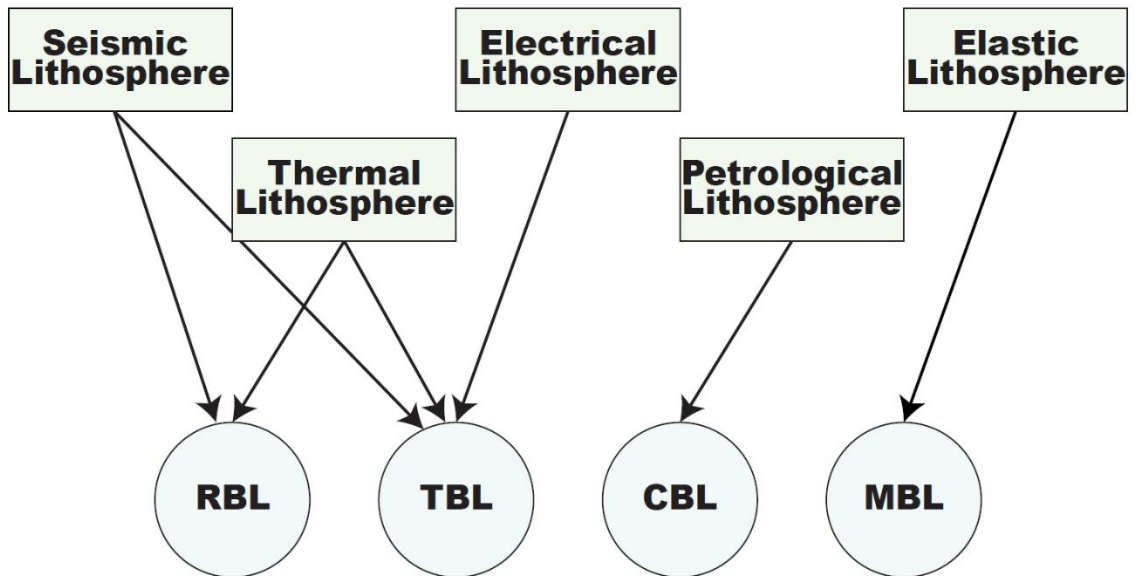


Figure 1. Relationships between different lithosphere definitions and boundary layers they define. RBL = Rheological Boundary Layer; TBL = Thermal Boundary Layer; CBL = Chemical Boundary Layer; MBL = Mechanical Boundary Layer. Adapted from Artemieva (2011).

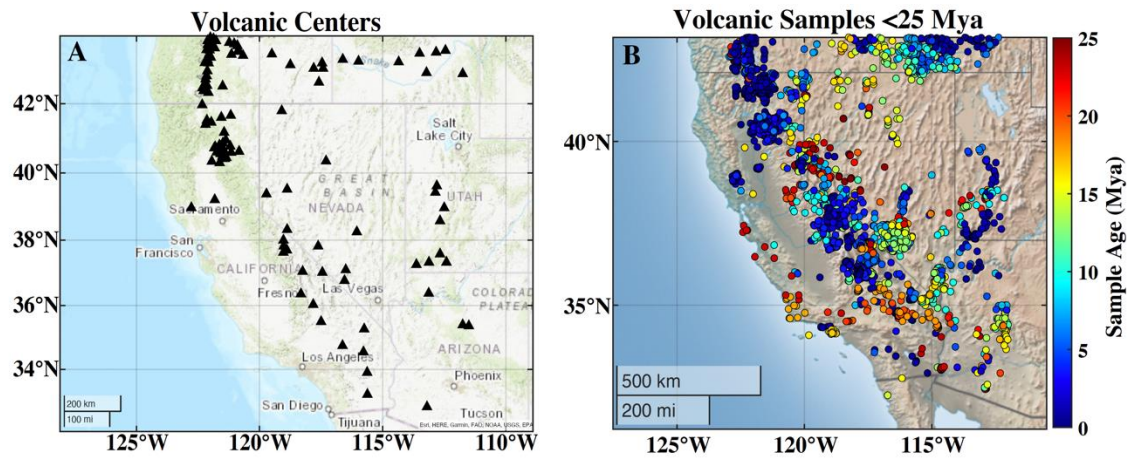


Figure 2. Map of volcanism in southwestern U.S. (a) Map of known volcanic centers, active and extinct, in the southwestern U.S. marked by black triangles. (b) Map of volcanic samples with calculated ages less than 25 Ma. Sample points colored by age, shown in color bar. Age and locations of samples collected from NAVDAT.

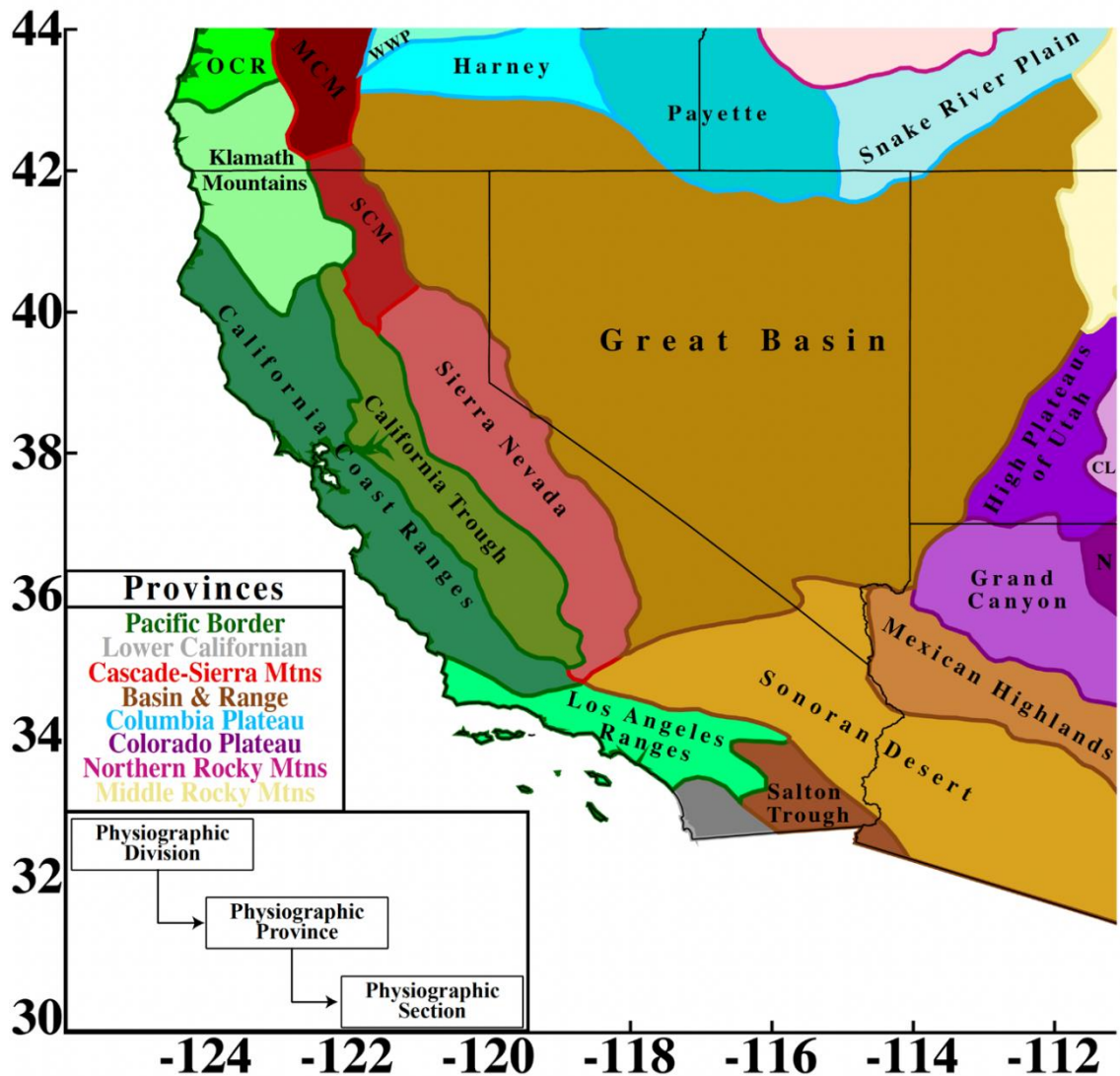


Figure 3. Province Map from Fenneman and Johnson (1946). Each province was assigned a main color, shown in the province list inset. Each section within a province was assigned a shade of the main color for its province. Inset of physiographic naming hierarchy in bottom left corner of map. Hierarchy from Fenneman and Johnson (1946), in which we focus on provinces and sections since divisions cover larger areas of land. Section name abbreviations: OCR = Oregon Coast Ranges; MCM = Middle Cascade Mountains; SCM = Southern Cascade Mountains; WWP = Walla Walla Plateau; CL = Canyon Lands; N = Navajo.

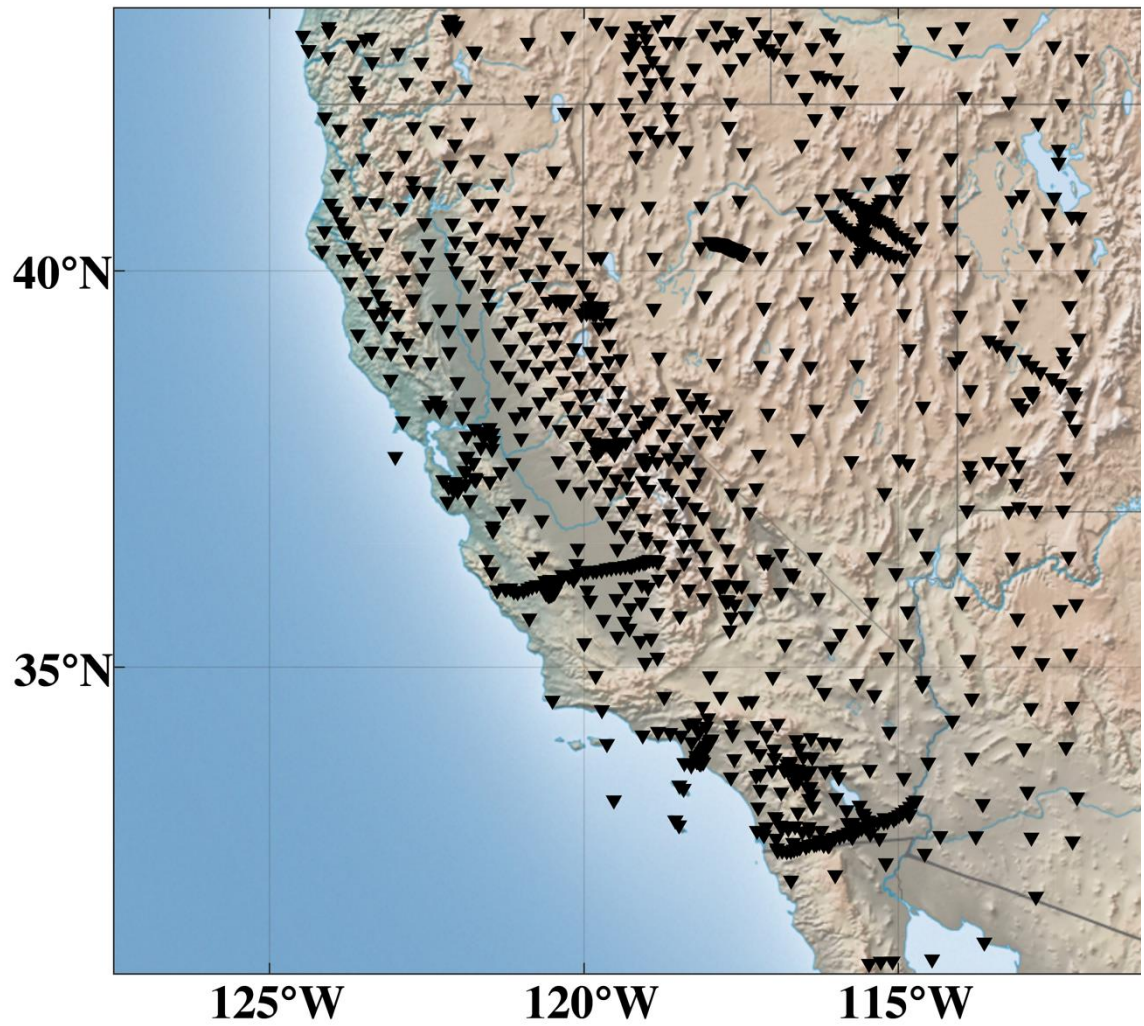


Figure 4. Station Map. Location of stations used for generation of receiver functions. Inverted black triangles represent broadband stations which recorded data within a time window from January 1980 to April 2021. All data used was accessed and downloaded through IRIS Data Management Center (DMC).

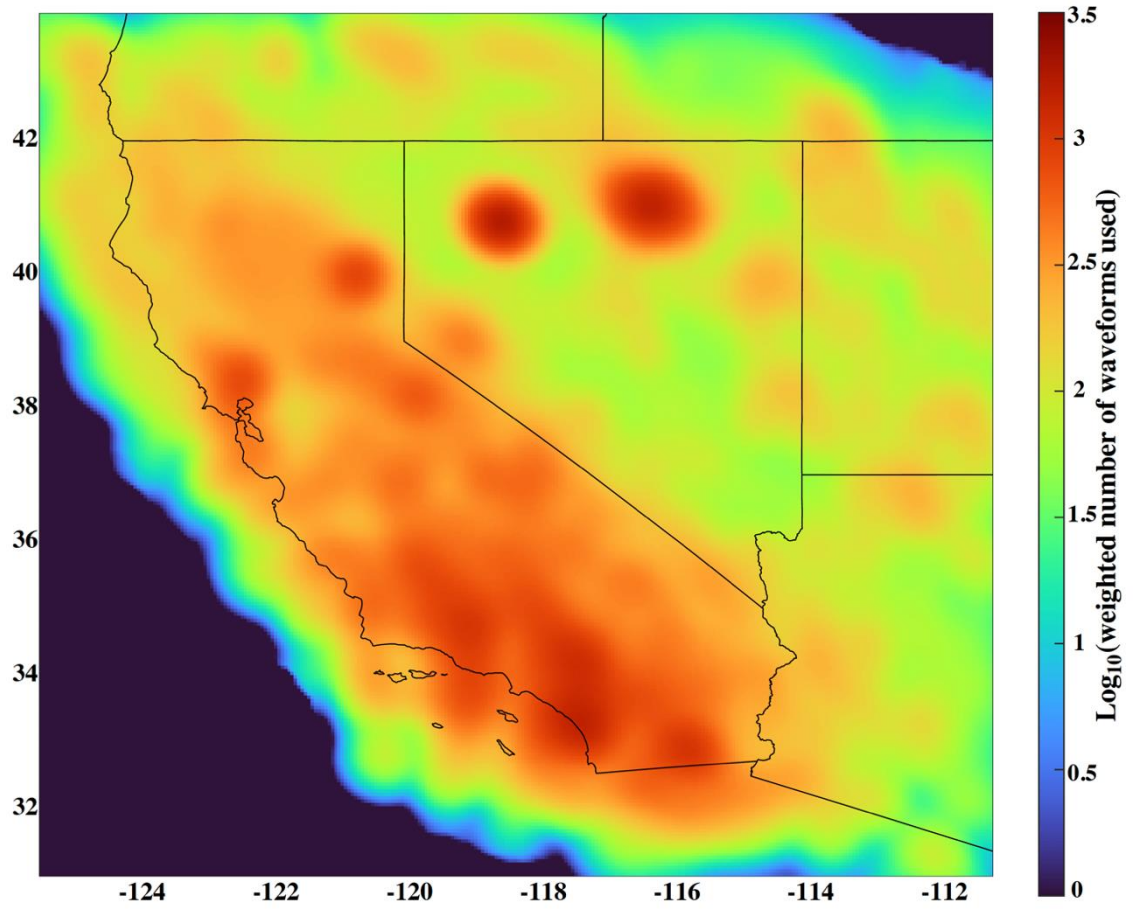


Figure 5. Coverage map of the logarithm of the weighted number of waveforms used in generation of receiver functions. Waveform coverage shown at 70 km depth. Weighted number of waveforms determined by weighting factor of Fresnel zones.

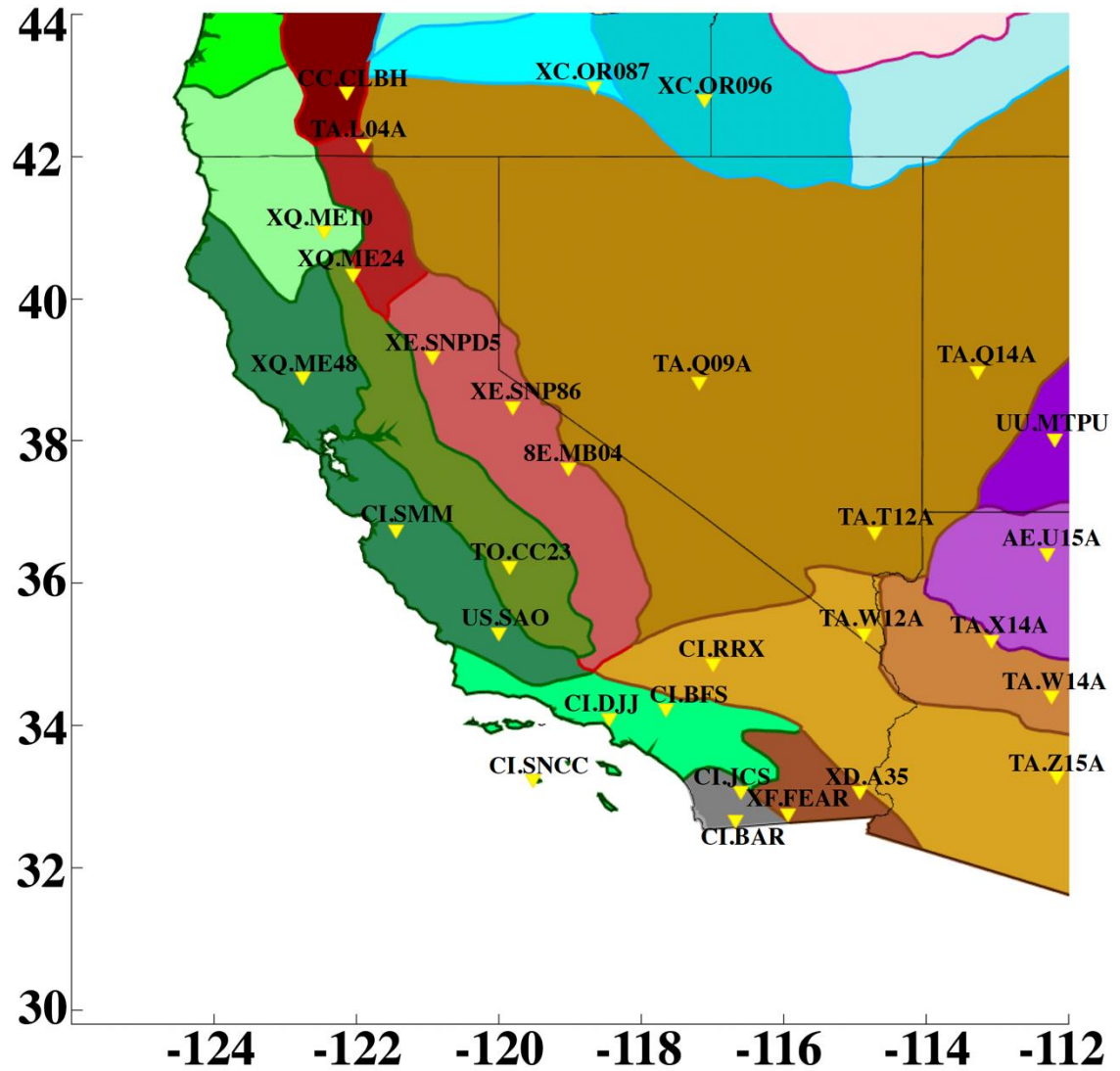
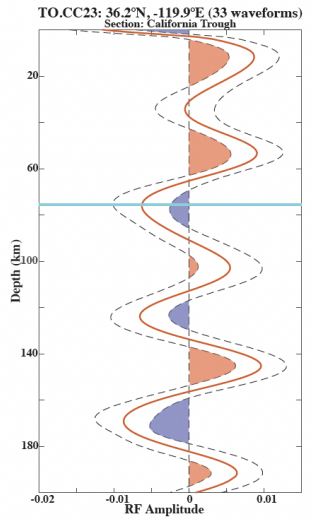
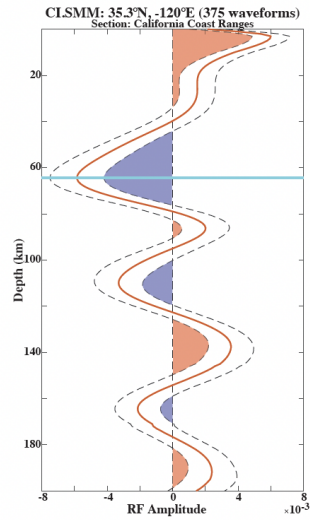
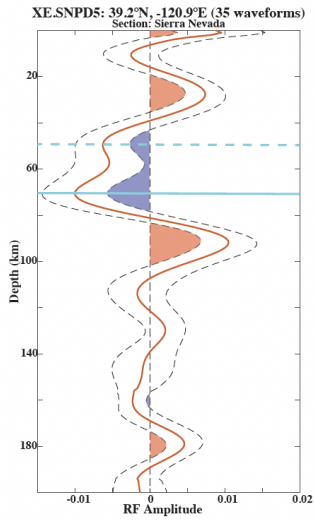
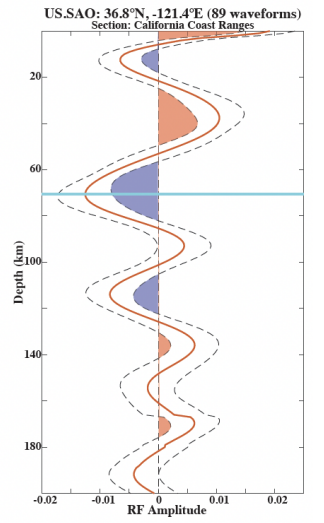
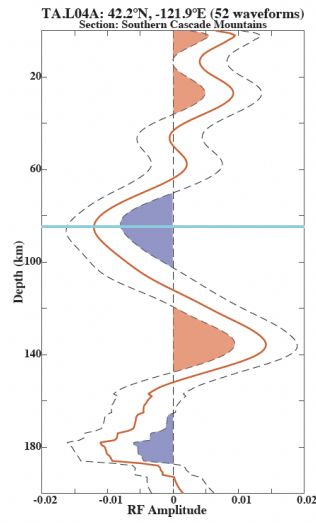
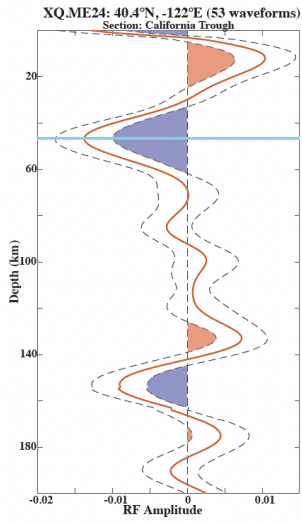
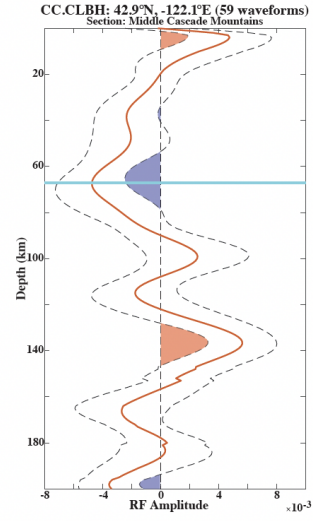
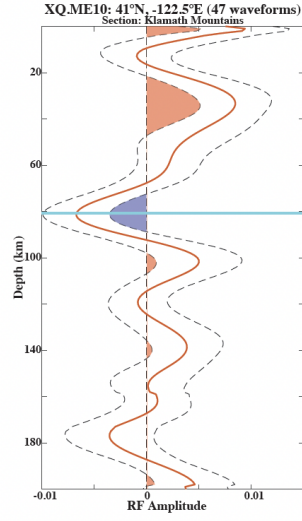
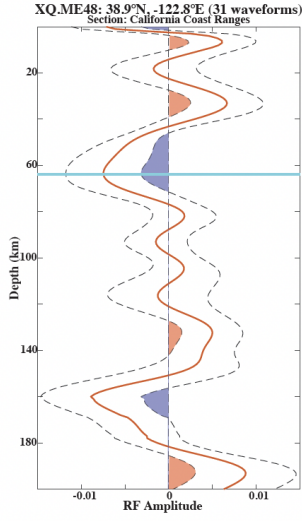
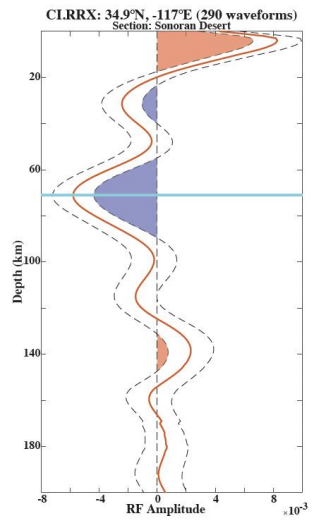
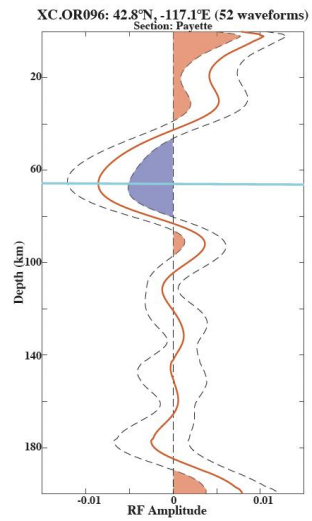
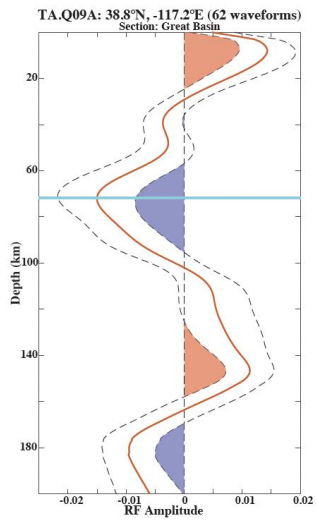
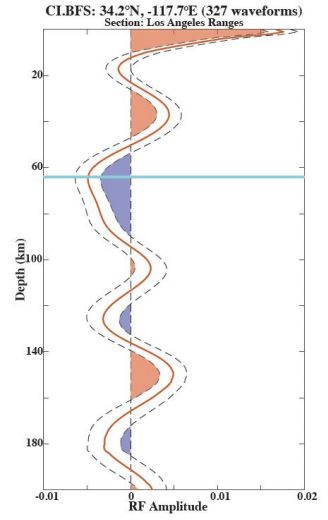
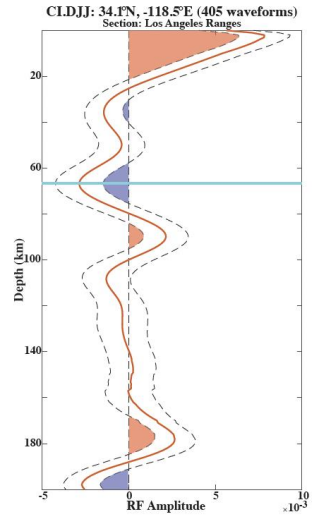
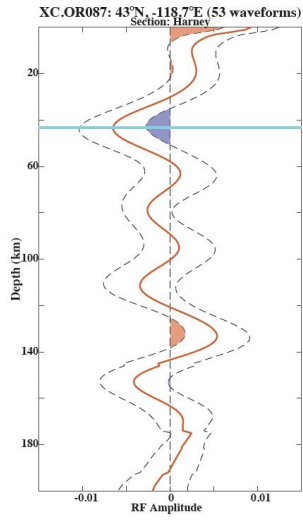
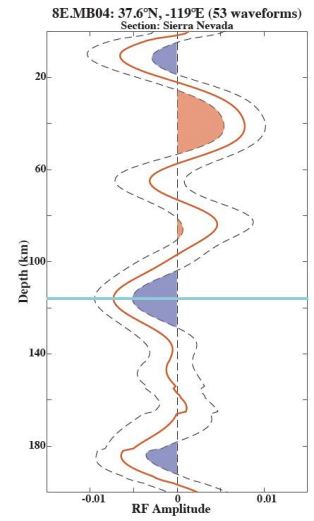
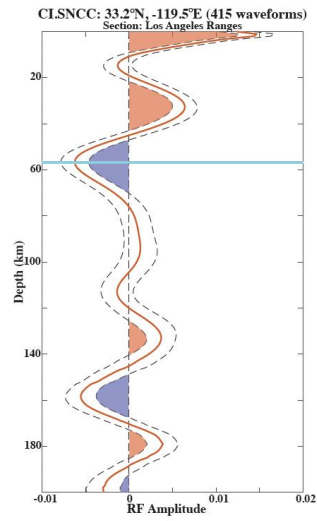
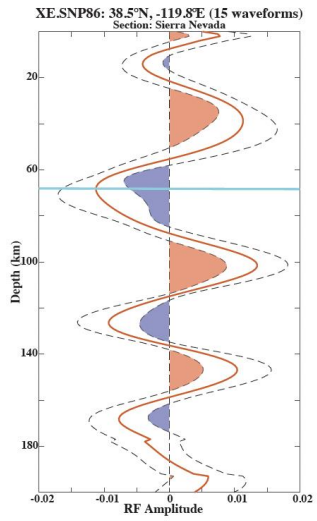
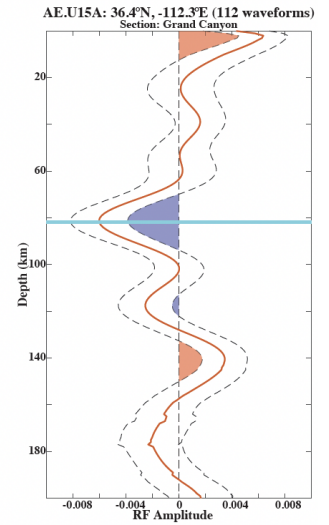
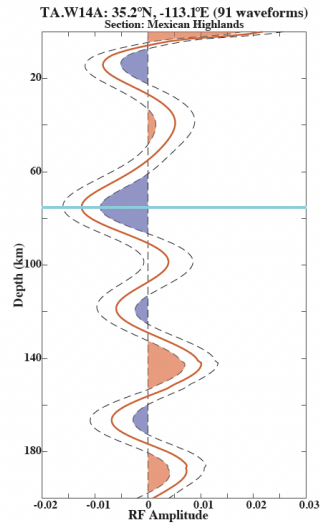
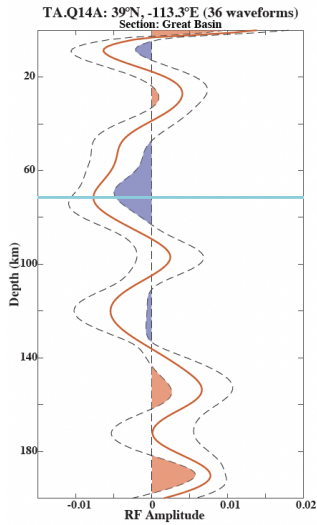
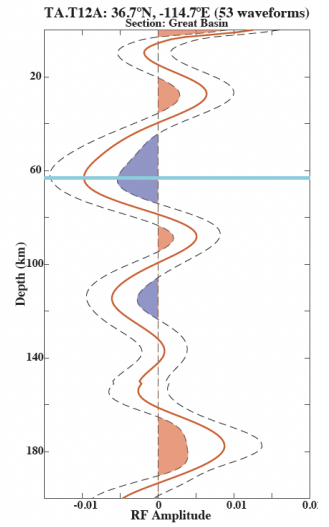
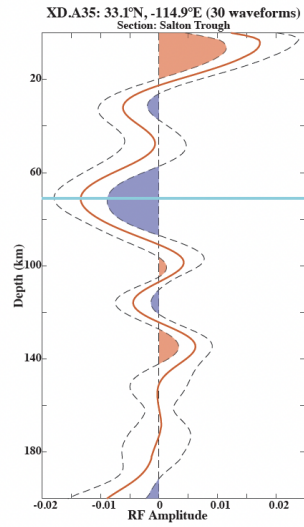
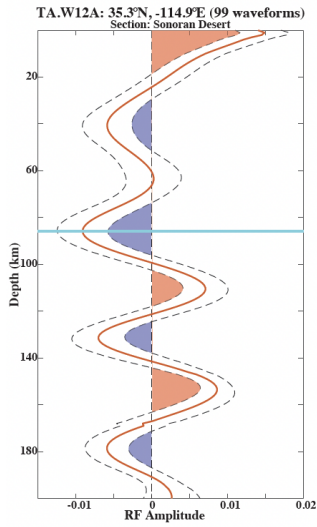
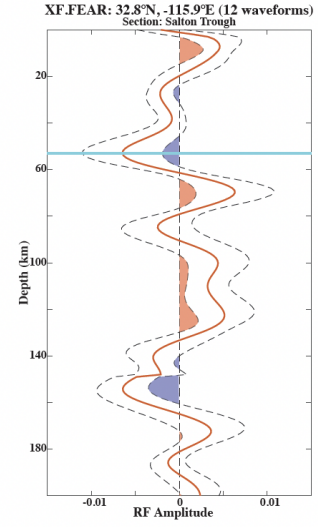
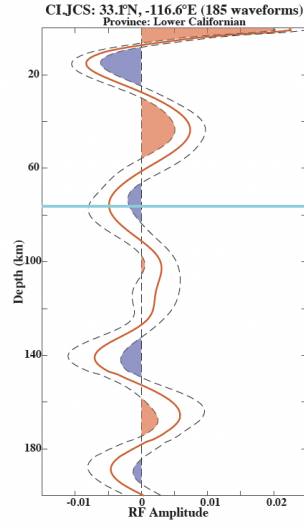
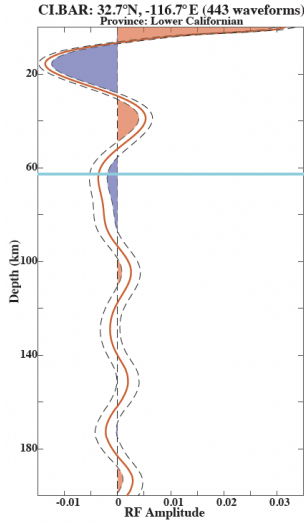


Figure 6. Locations of example single station stacked receiver functions. Inverted yellow triangles mark individual stations. Each station is labeled with network and station name. Stations picked to sample majority of physiographic sections and various areas within sections. Single station stacks are shown in Figure 7.







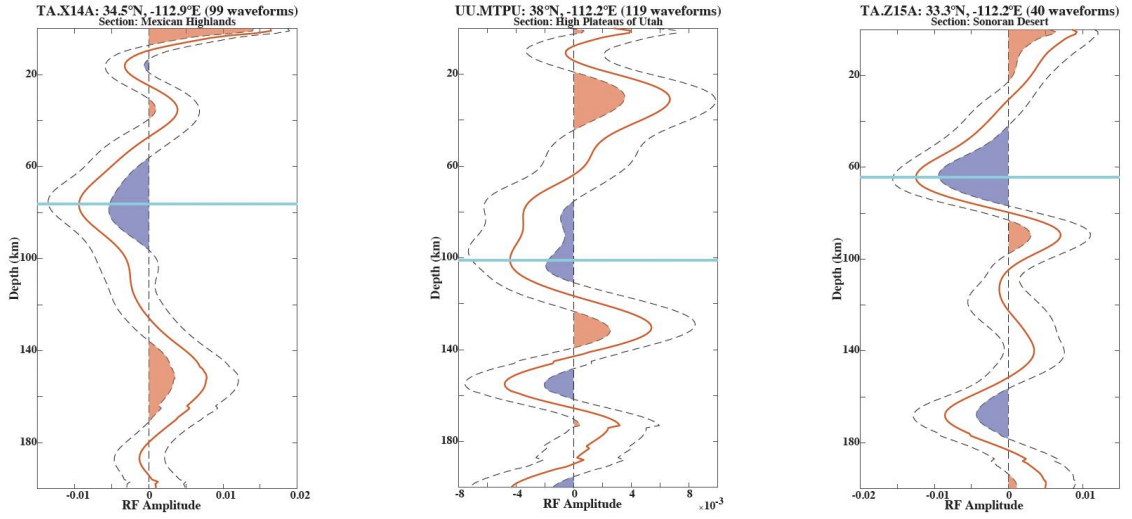


Figure 7. Example single station stacked receiver functions. Stacks are arranged in order of longitude from west to east, as well as from north to south (if they share the same longitude). Stacks are labeled with the network and station name, the number of waveforms used to generate the stack, and the physiographic section the stack corresponds to. Dashed black lines represent the 2σ uncertainty around the receiver function. Red phases correspond to statistically significant velocity increases with depth, while blue phases correspond to statistically significant velocity decreases with depth. Solid cyan lines denote the pick of the largest negative phase which meets our picking criteria. Dashed single cyan lines indicate a side lobe of the picked negative phase.

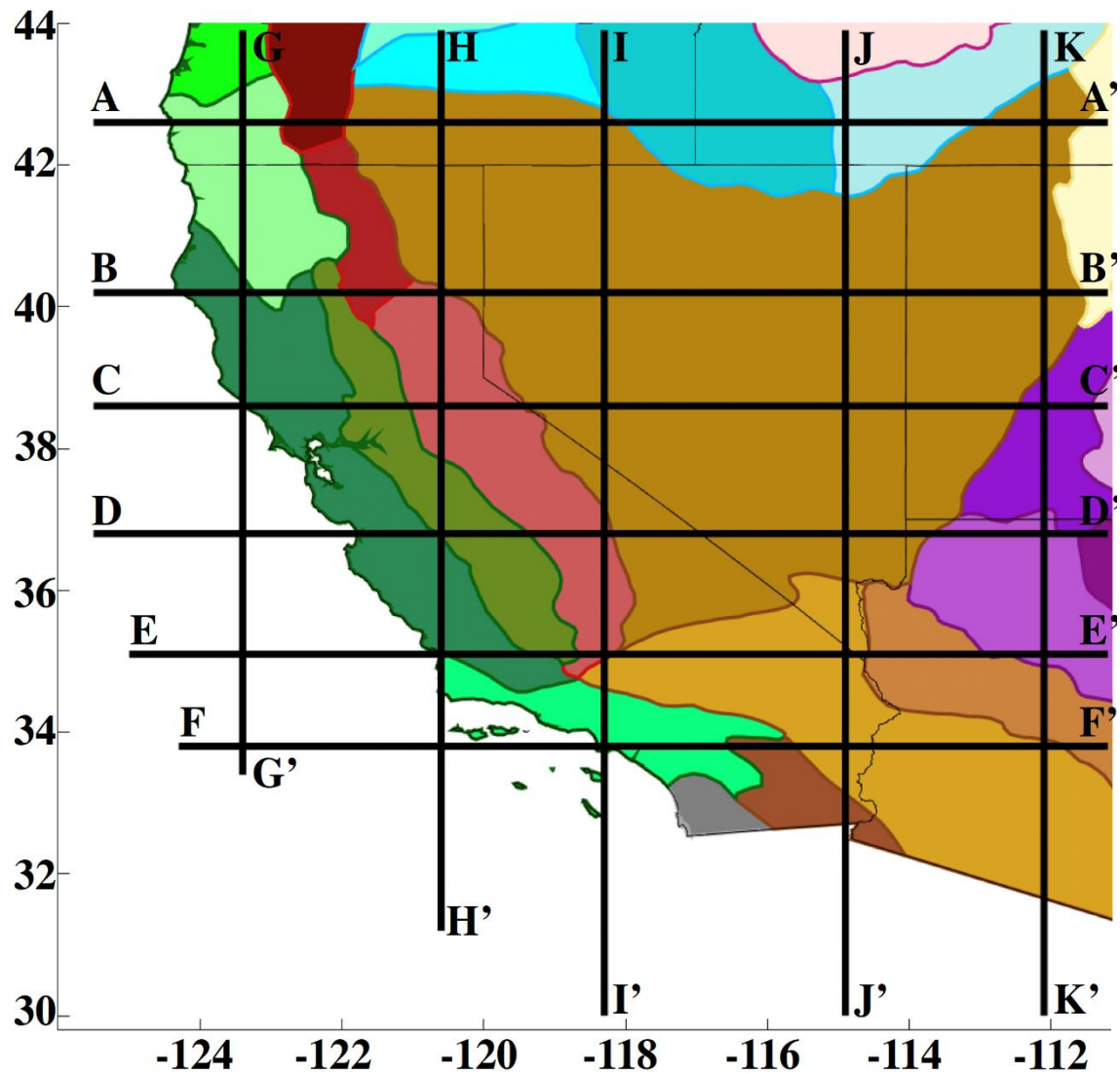
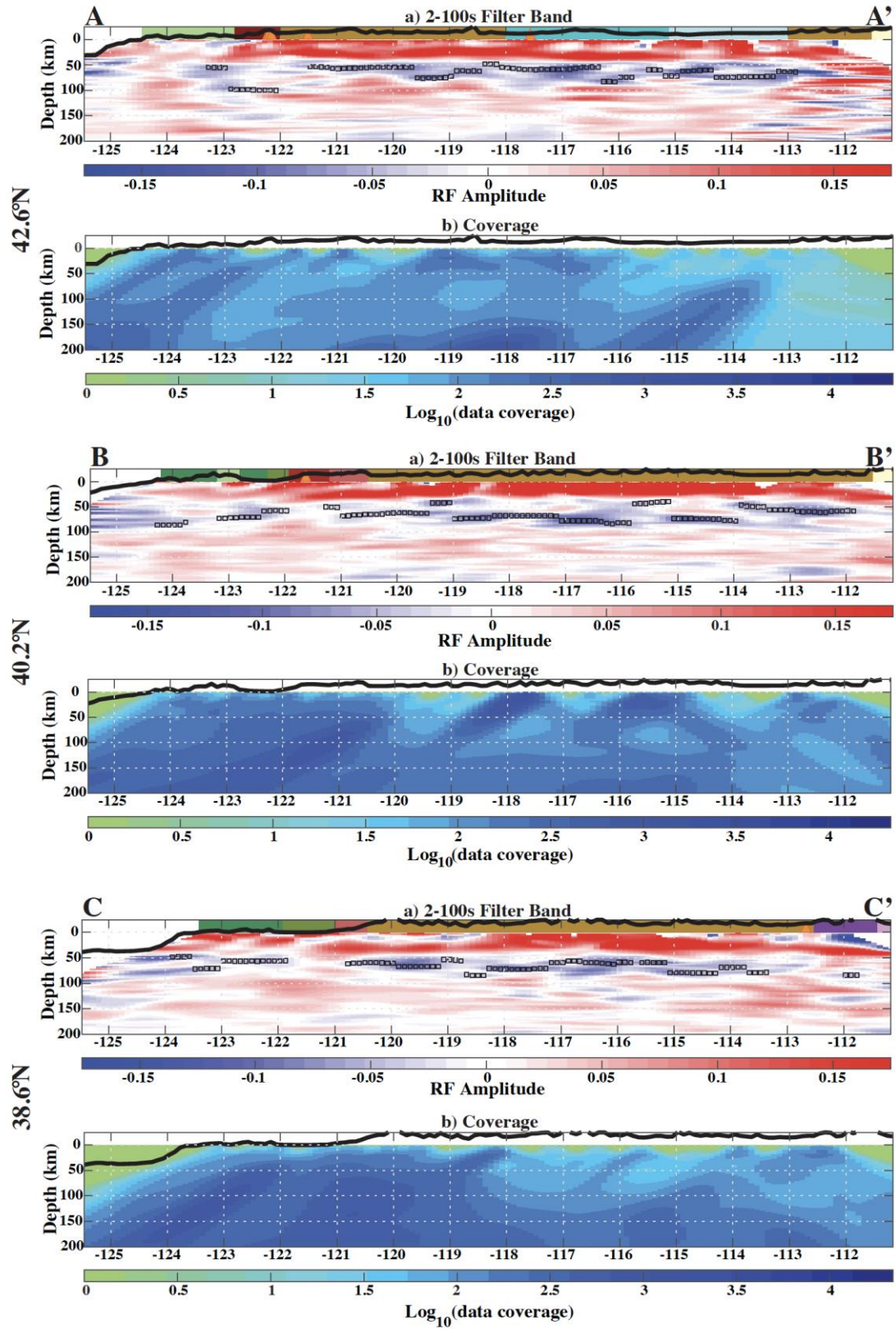


Figure 8. Map of cross section locations. Slices A through F are latitudinal (Figure 9) and slices G through K are longitudinal (Figure 10). Latitudinal sections are labeled west to east. Longitudinal sections are labeled north to south. For names of physiographic provinces and sections see Figure 3.



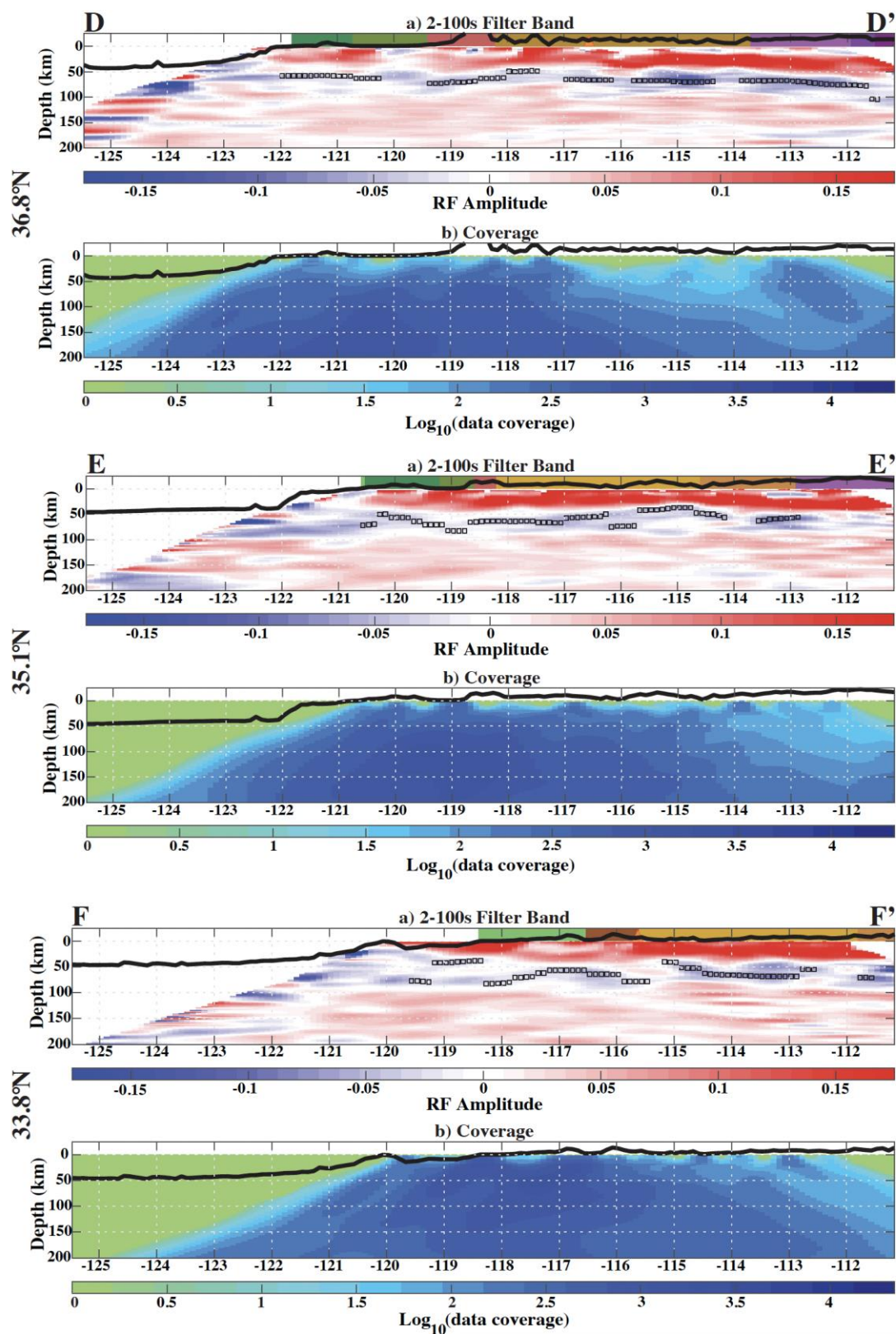
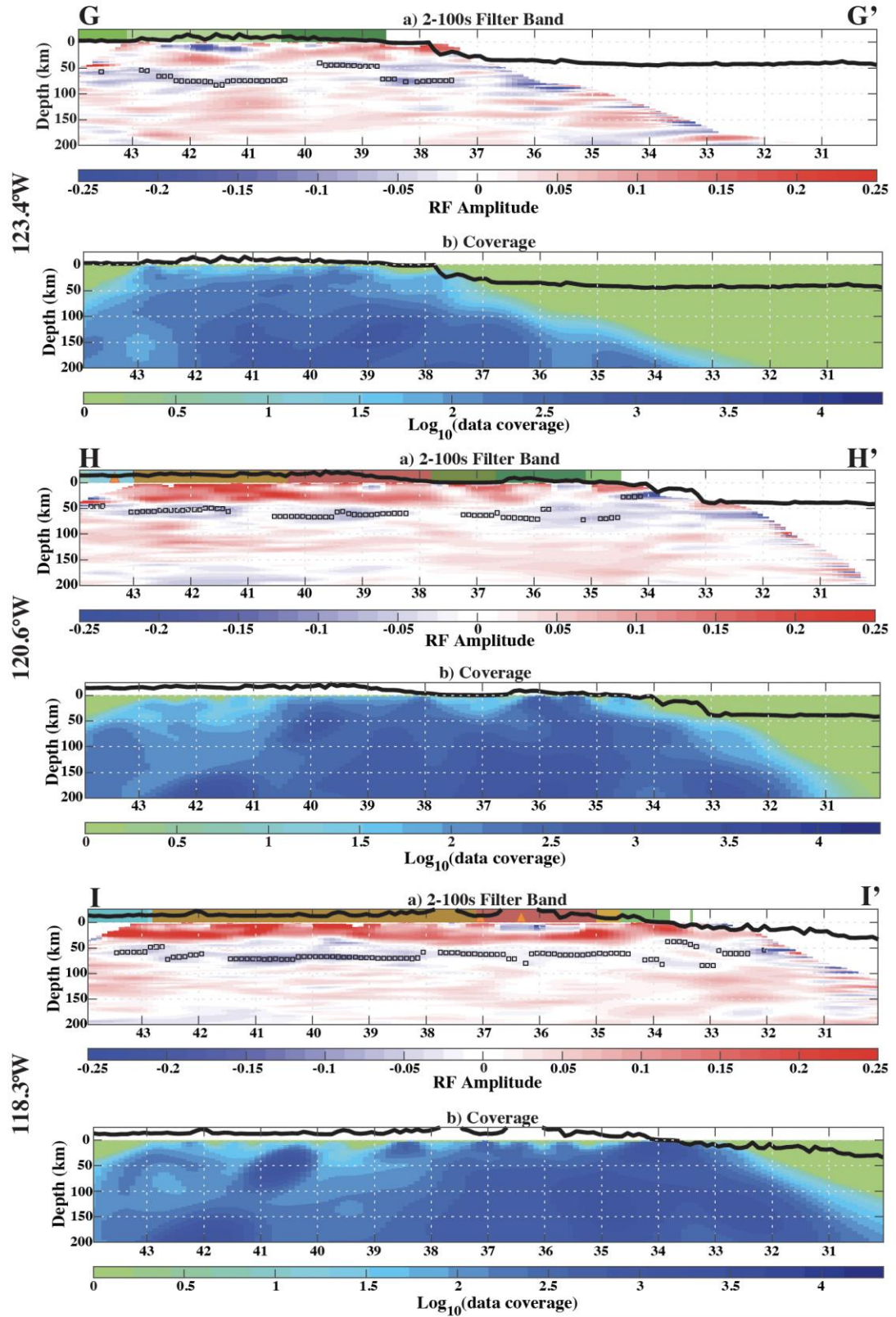


Figure 9. CCP slices and data coverage maps in depth for latitudinal cross sections A through F. In the CCP slice, red phases indicate velocity increases with depth while blue phases indicate velocity decreases with depth. Black boxes on stacks indicate handpicked negative phase. Topographic profiles at the top of each slice exaggerated by a factor of 10. Colors behind the topographic profiles in the CCP slices correspond to physiographic sections. Orange triangles on A-A', B-B', C-C', and F-F' represent volcanic centers from Figure 2(a) which fall within 0.1° of the cross section.



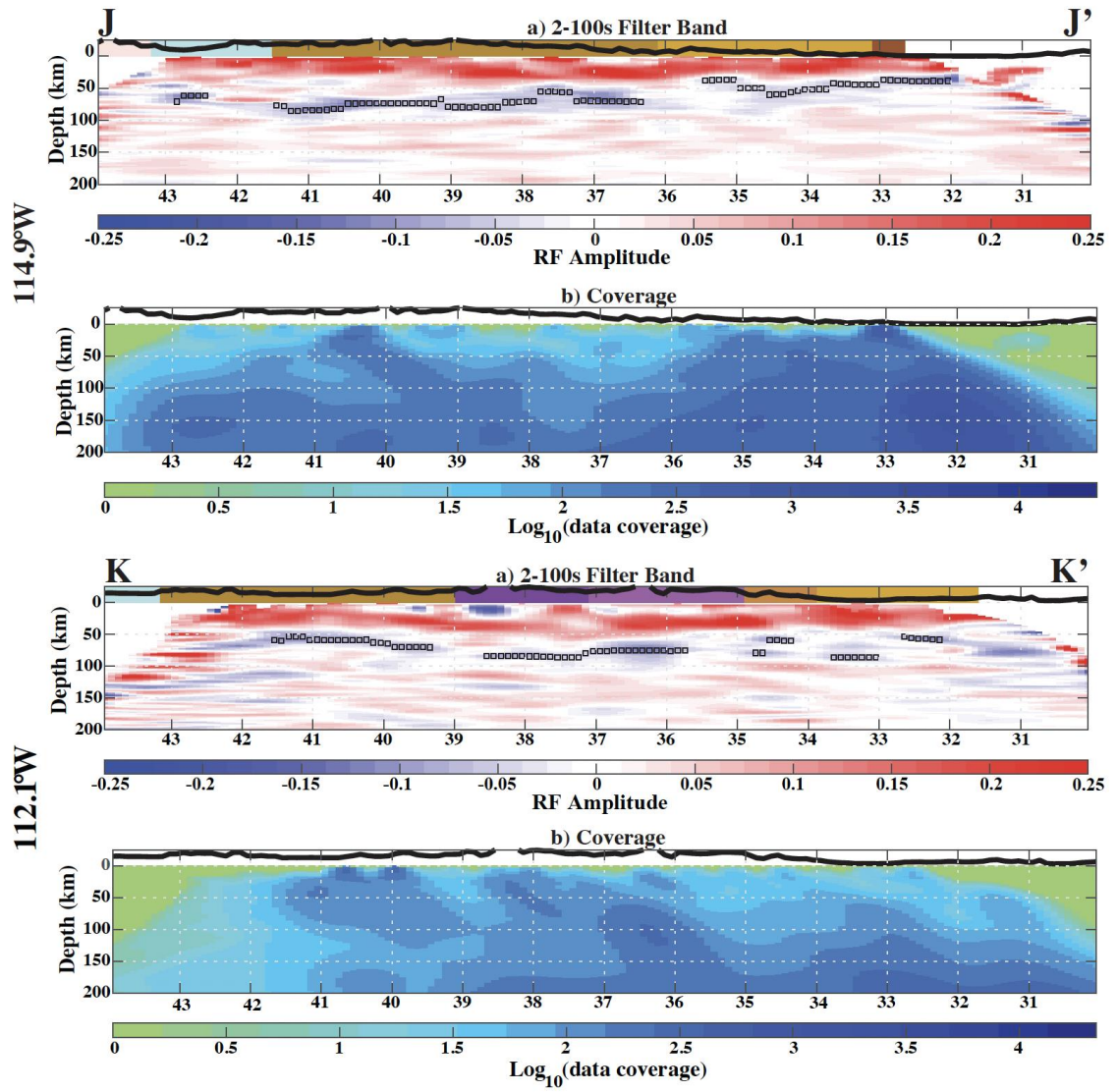


Figure 10. CCP slices and data coverage maps in depth for longitudinal cross sections G through K. Figure description same as for Figure 9.

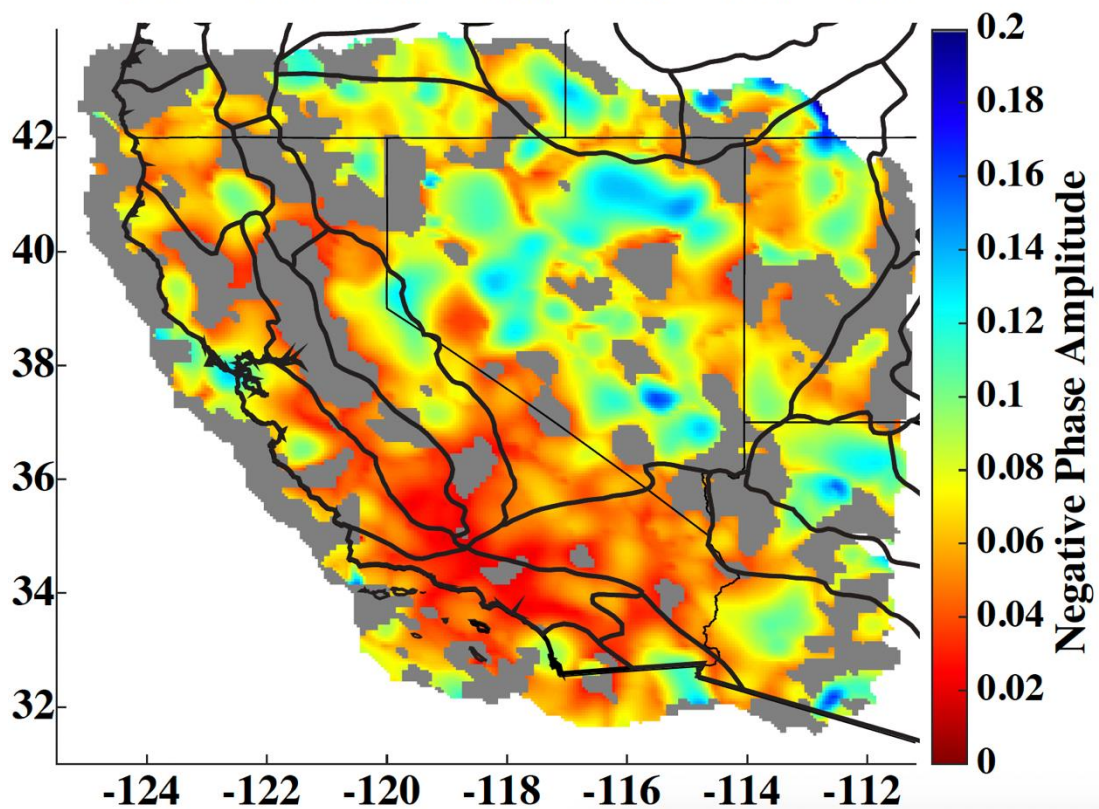
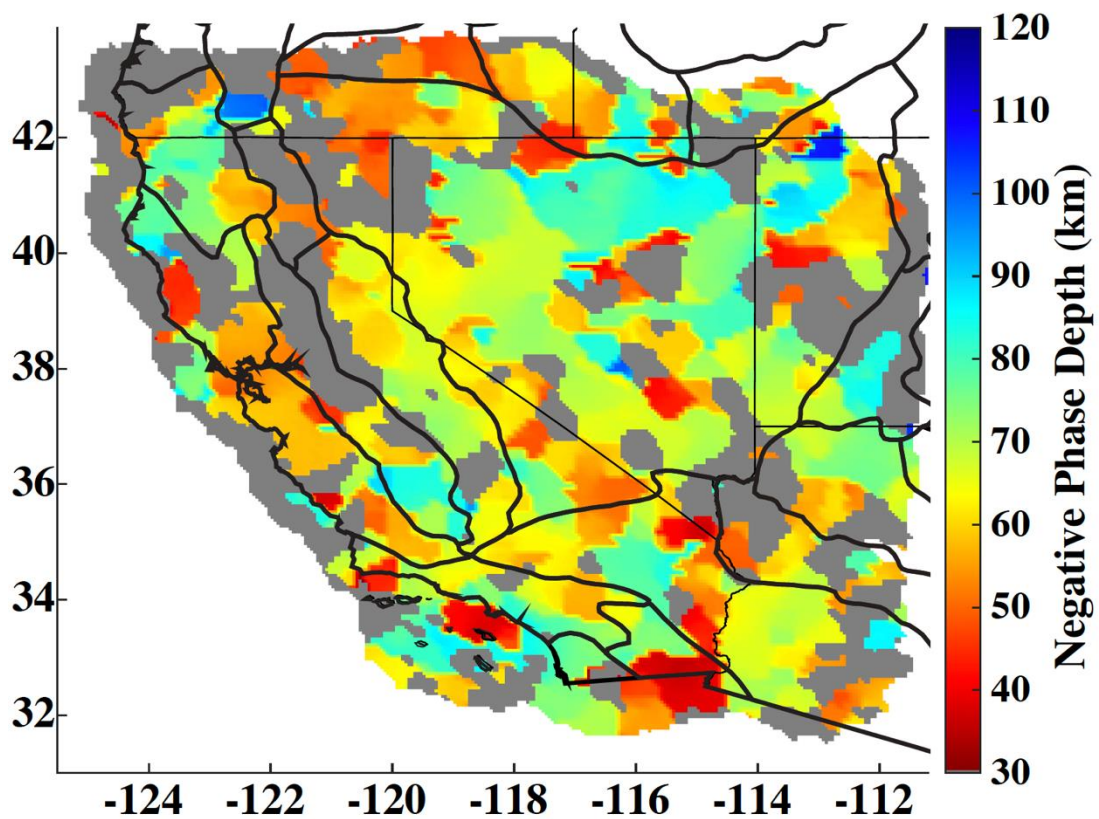


Figure 11. Results from hand picking the largest amplitude negative phase at each location. Gray regions on map correspond to locations where no pick was made. Dark black lines depict location of physiographic sections. (top) Map view of hand-picked negative phase depths. (bottom) Map view of amplitudes associated with hand-picked negative phases.

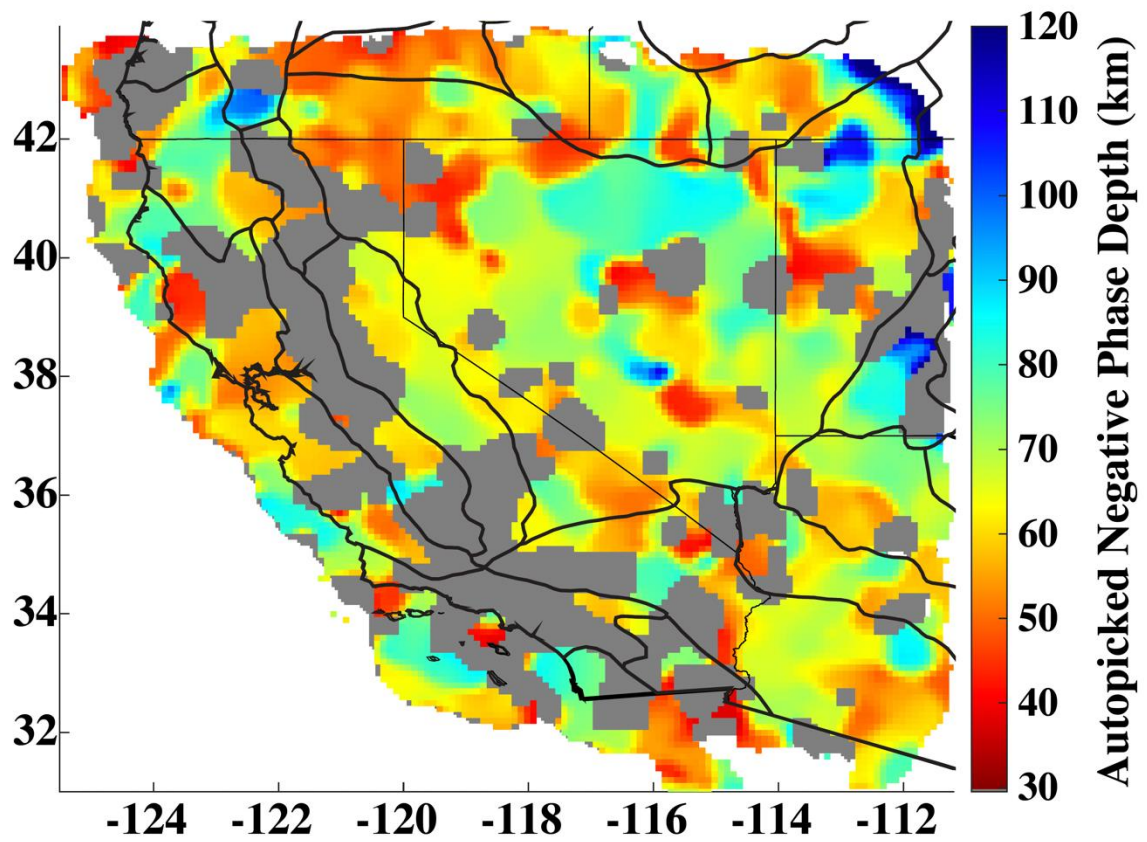


Figure 12. Depth of negative phase from autopicking function. Gray regions correspond to locations where a negative phase was not picked (based on parameters of picking function). Dark black lines depict location of physiographic sections.

Pacific Border Province

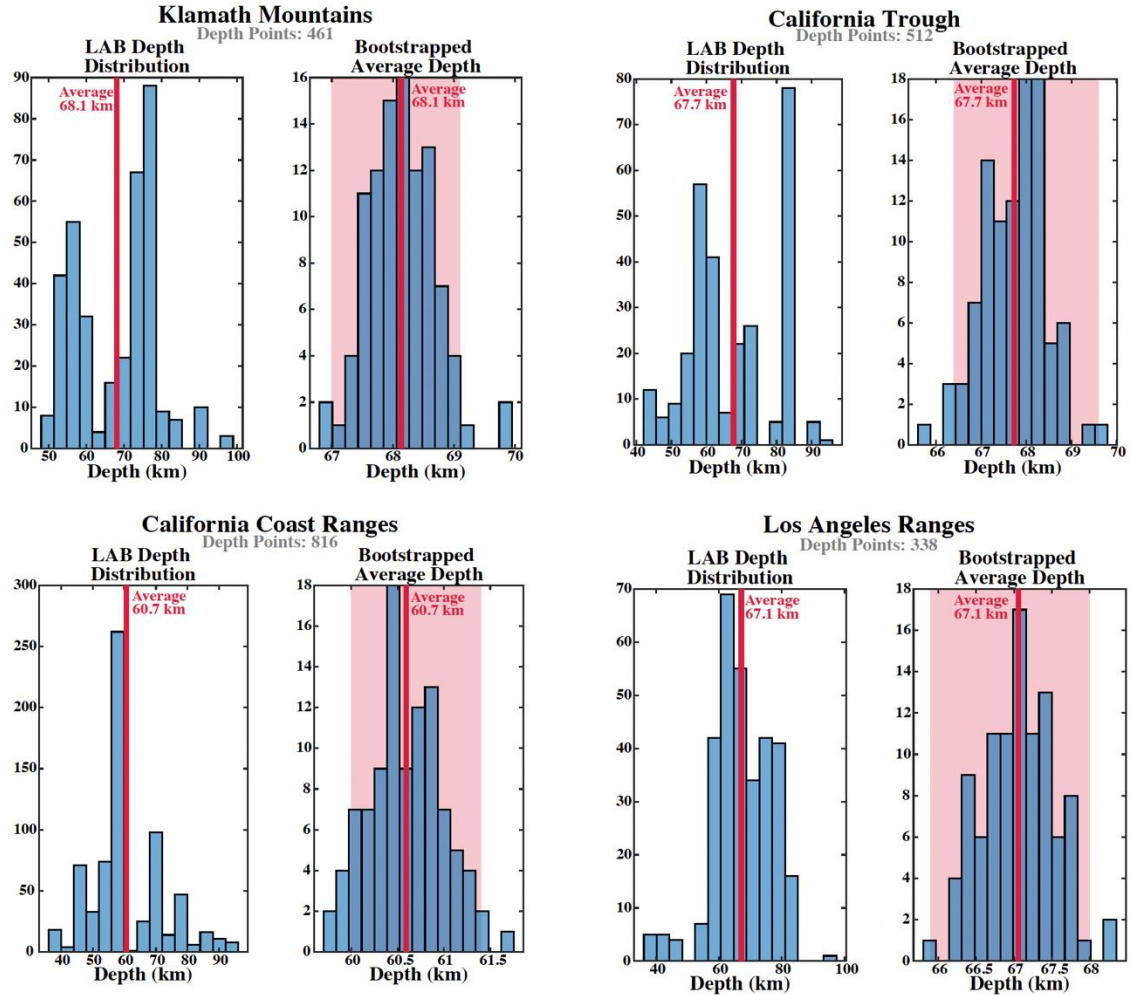


Figure 13. Depth distributions of the LAB picks and bootstrapped averages for the Pacific Border Province. Histograms for the physiographic sections in the following order: Klamath Mountains (top left), California Trough (top right), California Coast Ranges (bottom left), Los Angeles Ranges (bottom right). Oregon Coast Ranges not included due to a lack of picked negative phases. Each section has the number of depth points labeled, however, this includes NaN phase values which are not shown in the distribution. Average depth in both distributions, calculated as the non-NaN mean, is marked with a solid red line and labeled. Shaded red region in bootstrapped distributions represents the 95% confidence interval for the bootstrapping process for determining the average depth from the phase picks.

Cascade-Sierra Mountains

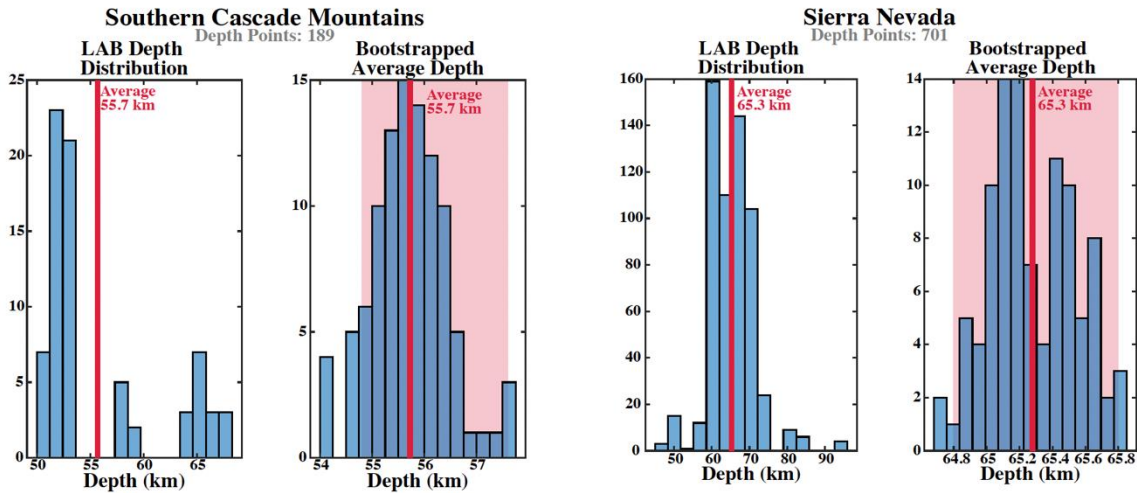


Figure 14. Depth distributions of the LAB picks and bootstrapped averages for the Cascade-Sierra Province. Histograms for the physiographic sections in the following order: Southern Cascade Mountains (left), Sierra Nevada (right). Middle Cascade Mountains not included due to a lack of picked negative phases. See Figure 13 for remaining description.

Basin & Range

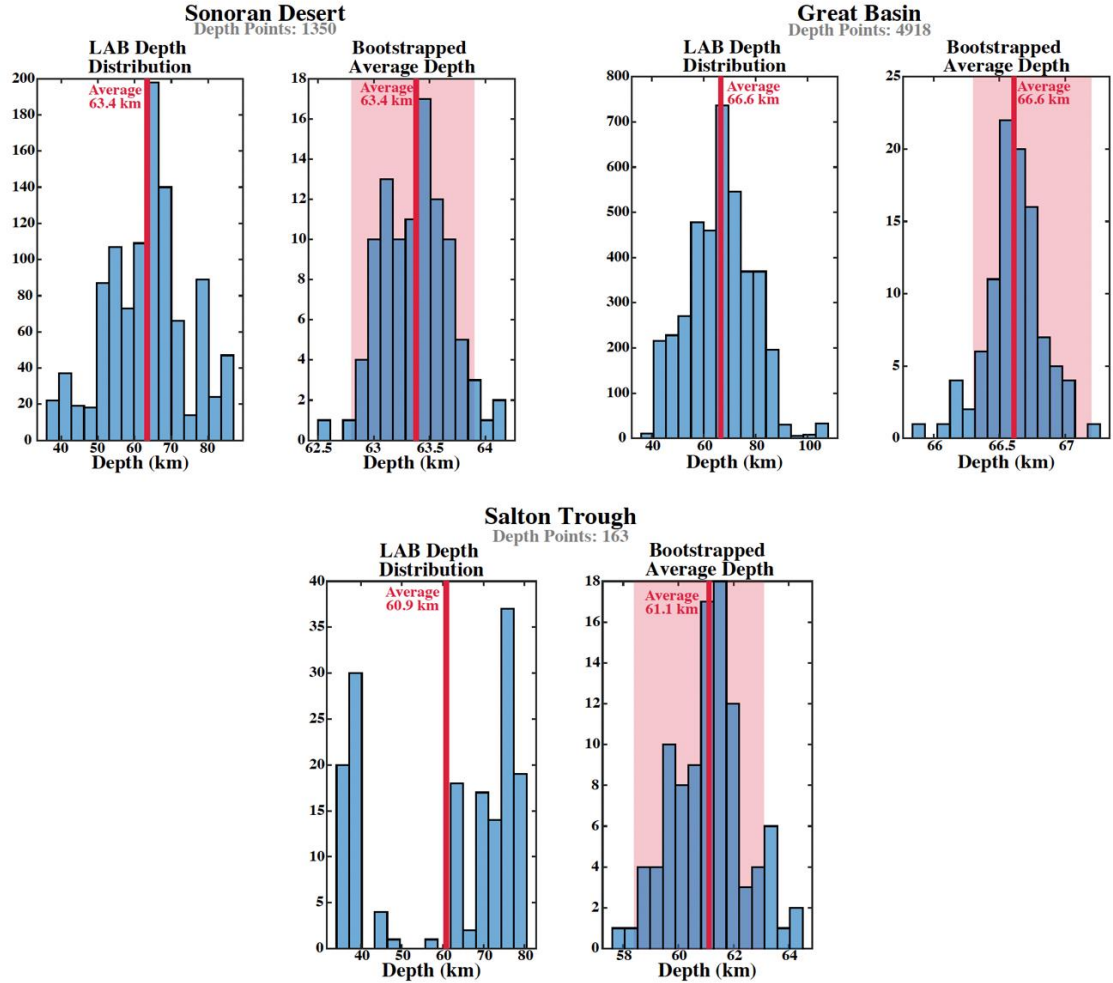


Figure 15. Depth distributions of the LAB picks and bootstrapped averages for the Basin and Range Province. Histograms for the physiographic sections in the following order: Sonoran Desert (top left), Great Basin (top right), Salton Trough (bottom center). Mexican Highlands not included due to a lack of negative phase picks. See Figure 13 for remaining description.

Colorado Plateau

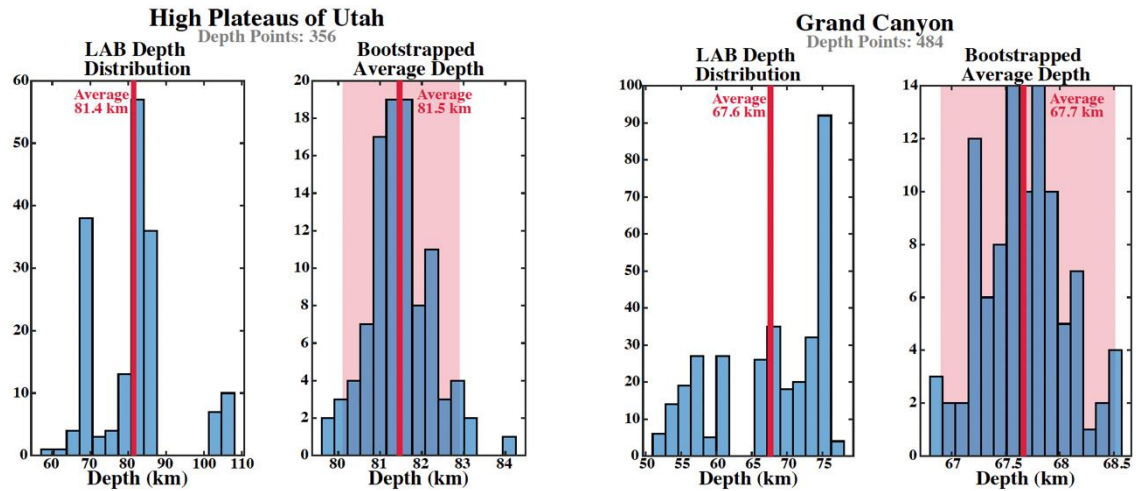


Figure 16. Depth distributions of the LAB picks and bootstrapped averages for the Colorado Plateau Province. Histograms for the physiographic sections in the following order: High Plateaus of Utah (left), Grand Canyon (right). Canyon Lands and Navajo not included due to location on the edge of study region. See Figure 13 for figure description.

Columbia Plateau

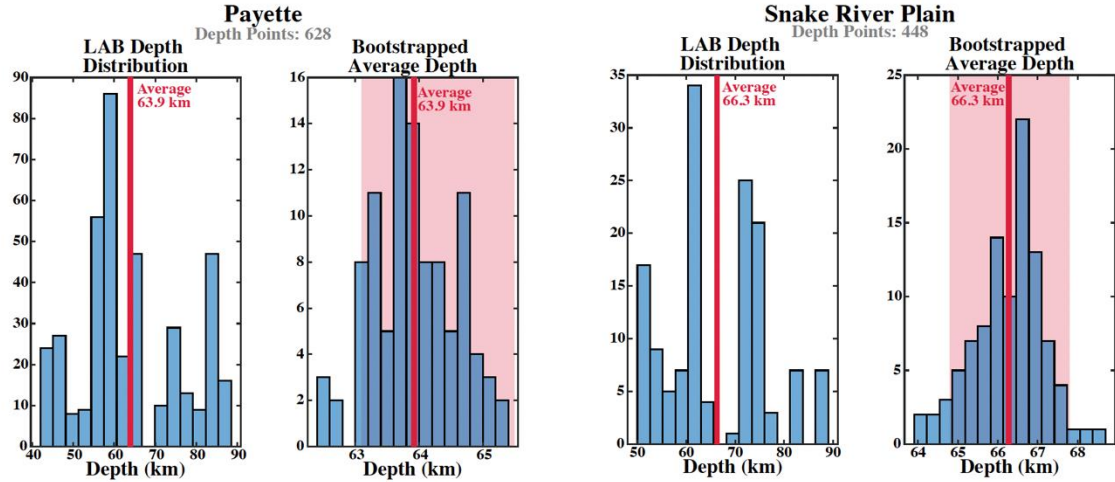


Figure 17. Depth distributions of the LAB picks and bootstrapped averages for the Columbia Plateau Province. Histograms for the physiographic sections in the following order: Payette (left), Snake River Plain (right). Harney and Walla Walla Plateau not included. See Figure 13 for description.

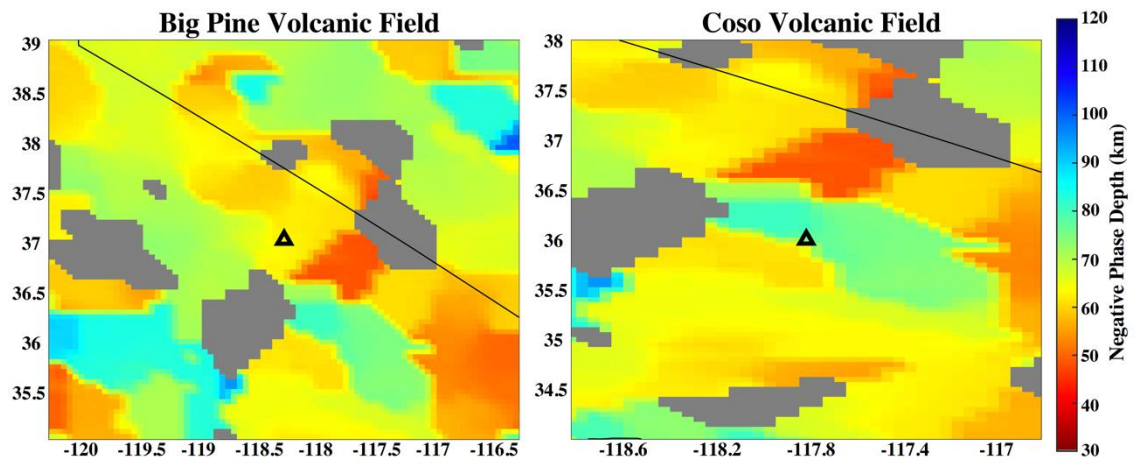


Figure 18. Map view of LAB depth surrounding (a) Big Pine Volcanic Field and (b) Coso Volcanic Field. Black triangle represents location of volcanic center. Black line north of volcanic centers is California-Nevada Border. Gray regions do not have phase picks for the LAB. LAB depth at Big Pine is 62.6 km; LAB depth at Coso is 76.8 km.

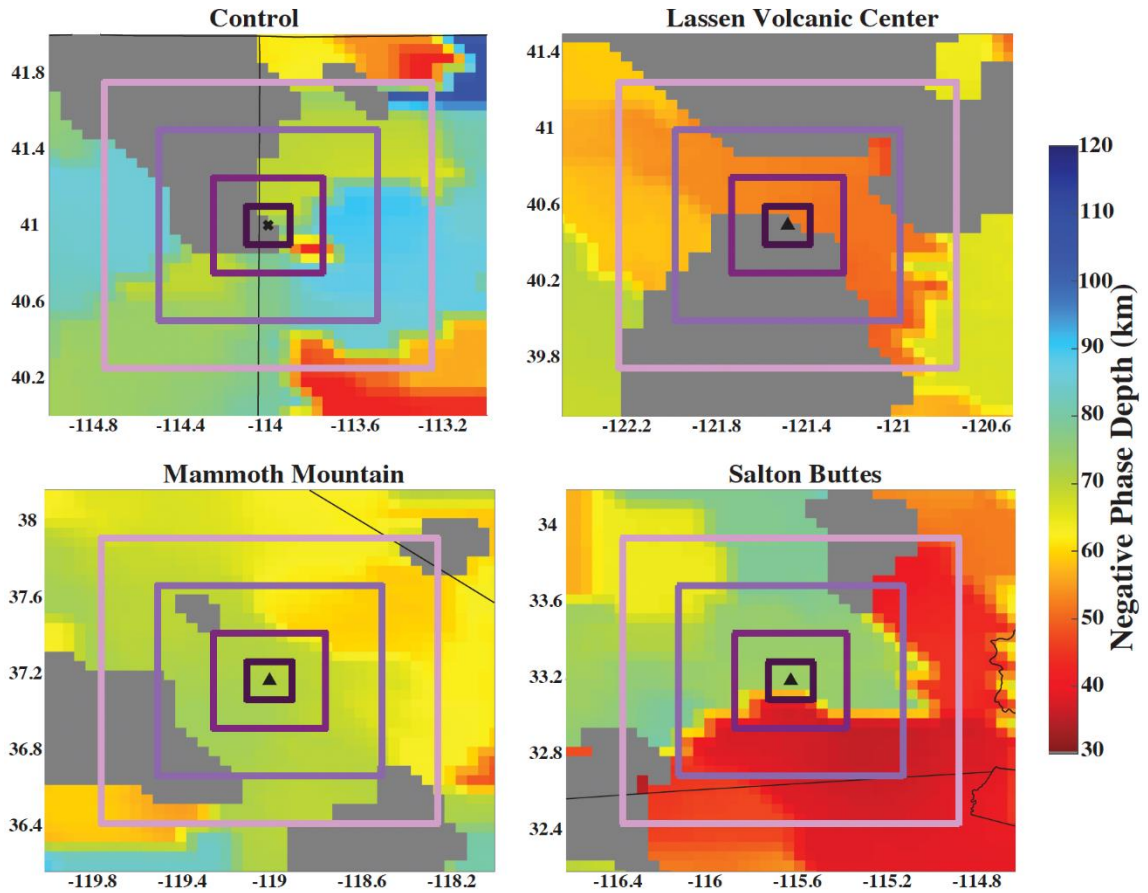
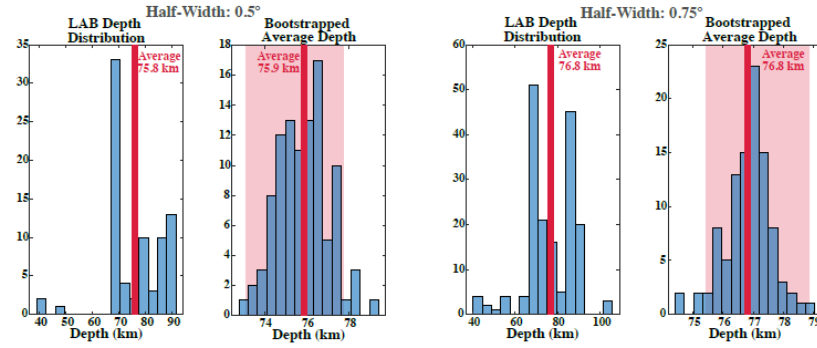
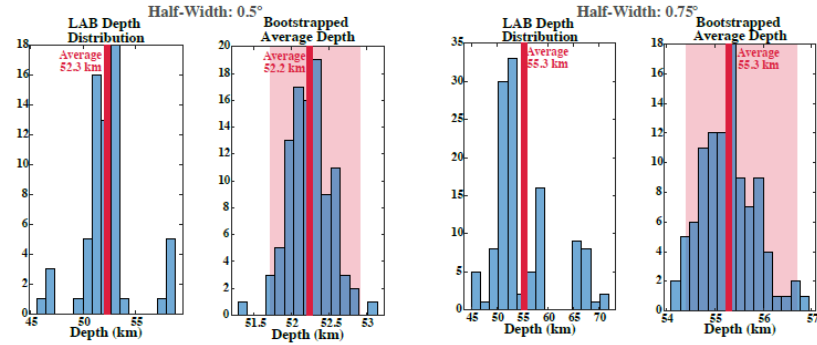


Figure 19. Map view of LAB depth at control region and volcanic centers. Purple boxes represent search boxes of various half-widths (0.1° , 0.25° , 0.5° , 0.75°). Gray regions represent locations where no LAB phase was picked. (a) Black “x” marks center of control region. Black line to west of center is Nevada-Utah border. (b-d) Black triangle represents location of volcanic center which half-widths are centered around. (b) Lassen Volcanic Center. Majority of the region does not have negative phase picks. (c) Mammoth Mountain. Black line in top right corner of map is California-Nevada border. (d) Salton Buttes. Black line to the south of the volcanic center is the California-Mexico border. Black line to the east is the California-Arizona border.

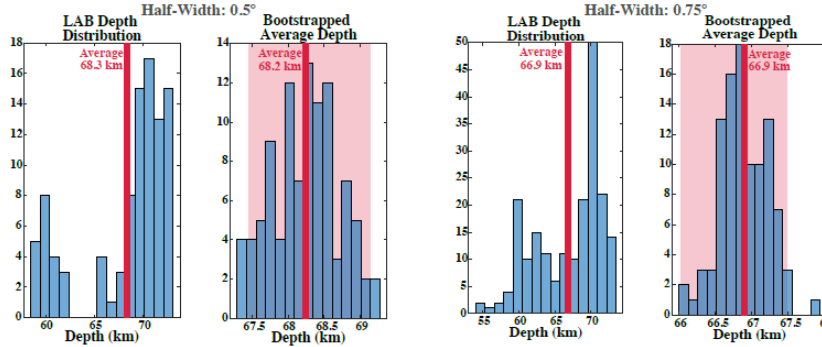
Control



Lassen Volcanic Center



Mammoth Mountain



Salton Buttes

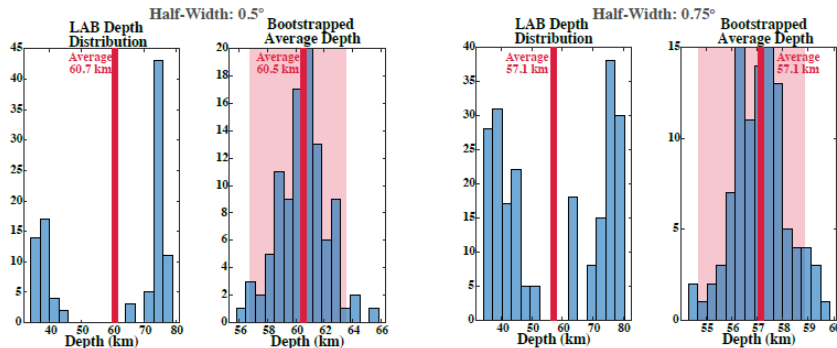


Figure 20. Depth distributions of the LAB picks and bootstrapped averages for half-widths of 0.5° and 0.75° for the control region and volcanic centers. The half-width of 0.5° has a maximum of 100 points and the half-width of 0.75° has a maximum of 225 points, however, this includes NaN values which are not shown in the distribution. Average depth in both distributions, calculated as the non-NaN mean, is marked with a solid red line and labeled. Shaded red region in bootstrapped distributions represents the 95% confidence interval for the bootstrapping process for determining the average depth from the phase picks.

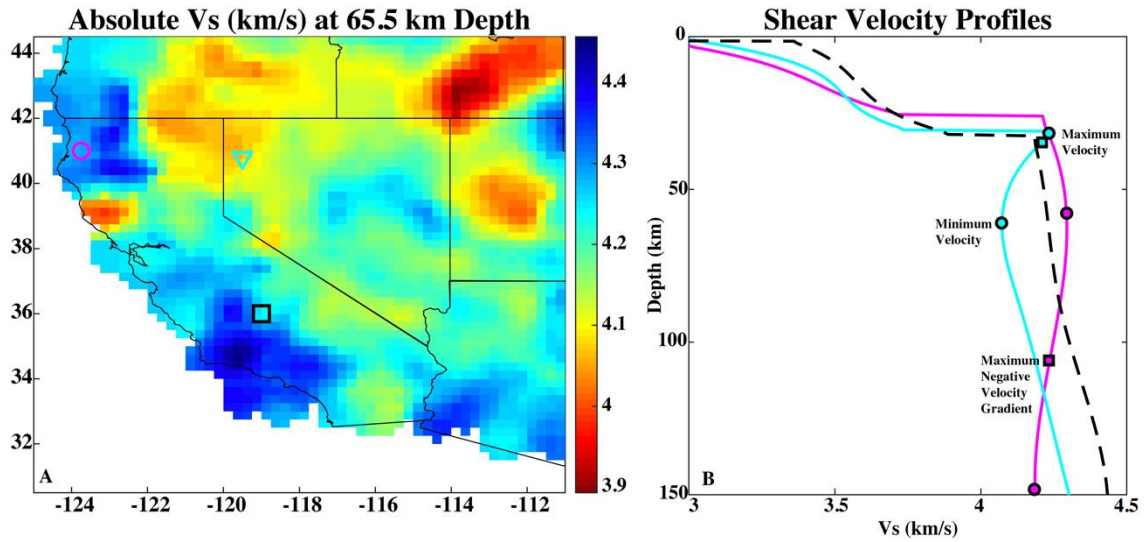


Figure 21. (a) Plot of shear velocity model (Shen & Ritzwoller, 2016) at 65.5 km depth. Blue colors correspond to faster wave speeds and red colors correspond to slower wave speeds. The location of three shear velocity profiles are marked by the magenta circle, cyan triangle and black square and are shown on the right. (b) Three examples of shear velocity profiles from Shen and Ritzwoller (2016). The Moho in each profile corresponds to the rapid increase in velocity at roughly 25-30 km depth. Marked by filled circles are the depths of the minimum velocities and maximum velocities for the cyan and magenta profiles. The filled squares mark the locations of the calculated maximum negative velocity gradients for the cyan and magenta profiles. No selections were made for the dashed profile as it exhibits no low velocity zone.

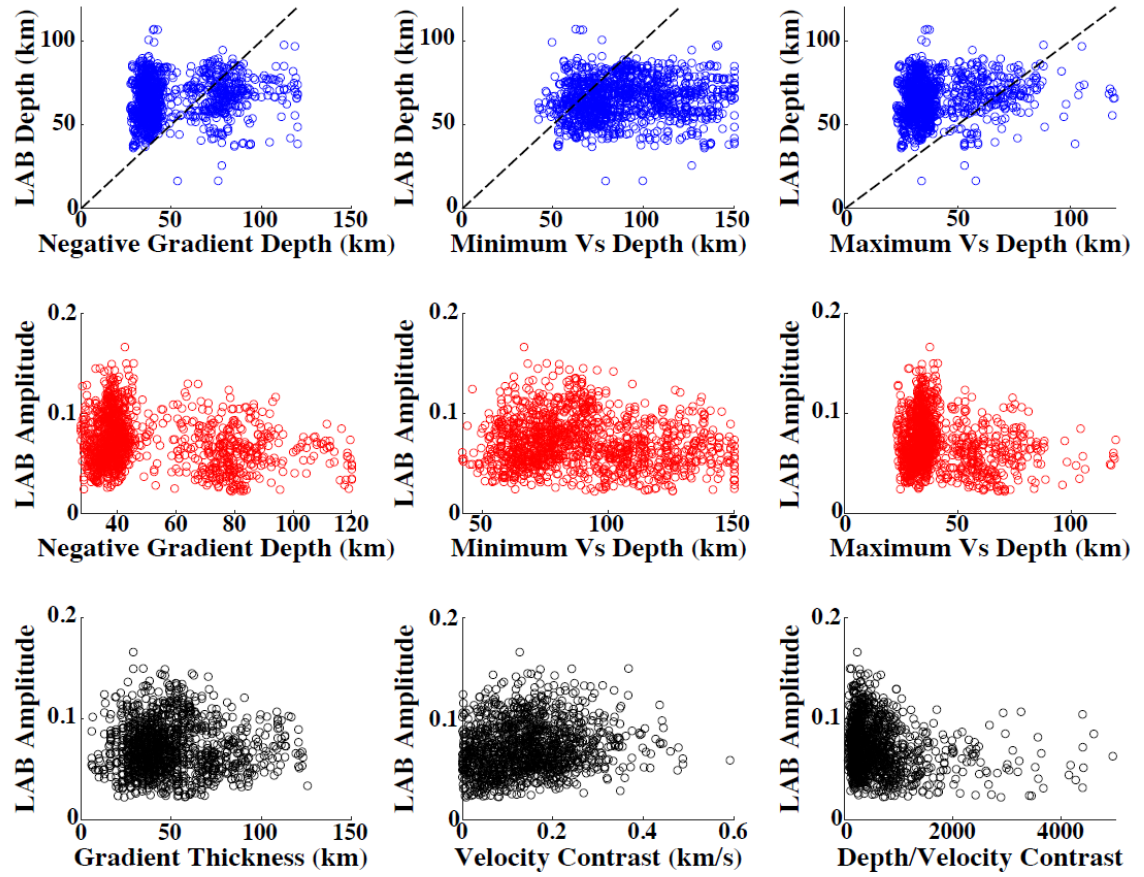


Figure 22. (top row) Comparison of LAB depth determined by Sp receiver function analysis to the negative of the (left) maximum negative velocity gradient, (center) minimum shear velocity depth and (right) maximum shear velocity depth, as determined from the tomography model of Shen and Ritzwoller (2016). Dashed line represents a 1:1 correlation. (center row) Comparison of LAB amplitude determined by Sp receiver function analysis and compared to the same tomographic measures as the top row. (bottom row) LAB amplitude compared to (left) gradient thickness, velocity contrast and the gradient thickness divided by velocity contrast, determined by taking the difference between the depths and velocities of the maximum and minimum shear velocities from Shen and Ritzwoller (2016).

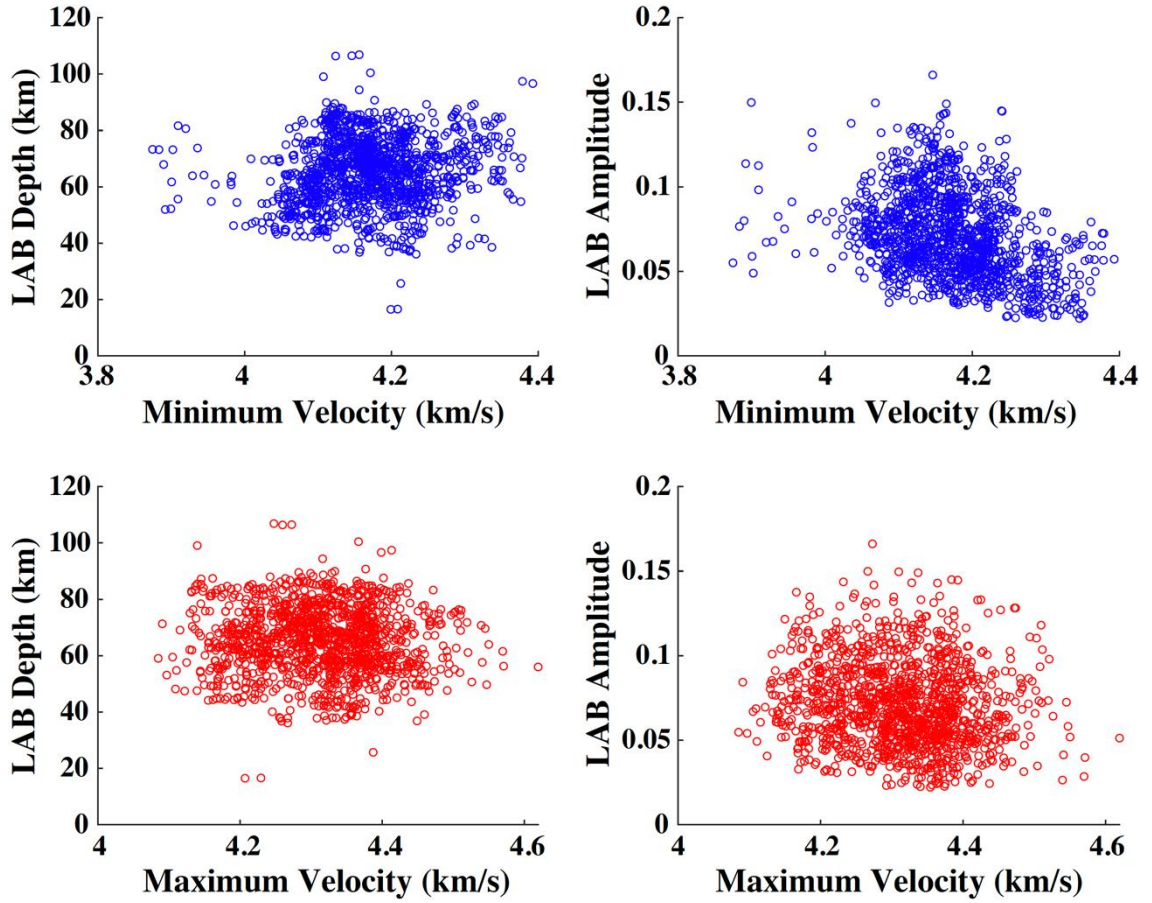


Figure 23. (left) Comparison of LAB depth determined by Sp receiver function analysis to the (top) minimum shear velocity and (bottom) maximum shear velocity, as determined from the tomography model of Shen and Ritzwoller (2016). (right) Comparison of LAB amplitude determined by Sp receiver function analysis and compared to the same measures as the left column.

Physiographic Province	Physiographic Section	Number of Depth Points	Unbootstrapped Values				Bootstrapped Values			
			Average Depth (km)	Maximum Depth (km)	Minimum Depth (km)	Depth Range (km)	Average Depth (km)	Maximum Depth (km)	Minimum Depth (km)	Depth Range (km)
Columbia Plateau	Walla Walla Plateau	39	49.8	49.8	49.8	0	49.8	49.8	49.8	0
	Payette	628	63.9	87.9	43.9	44.0	63.9	65.4	62.4	3.0
	Snake River Plain	448	66.3	88.7	50.0	38.7	66.3	68.6	63.9	4.7
Colorado Plateau	Harney	272	50.1	74.7	44.5	30.2	50.1	50.9	49.3	1.6
	High Plateaus of Utah	356	81.4	107.3	59.8	47.5	81.5	84.2	79.7	4.5
	Grand Canyon	484	67.6	77.6	51.1	26.5	67.7	68.6	66.9	1.7
Basin and Range	Navajo	45	71.7	77.6	66.2	11.4	71.6	74.1	68.9	5.2
	Great Basin	4918	66.6	107.4	38.1	69.3	66.6	67.3	65.9	1.3
	Sonoran Desert	1350	63.4	86.8	36.6	50.2	63.4	64.2	62.5	1.7
Cascade-Sierra Mountains	Salton Trough	163	60.9	80.0	35.7	44.3	61.1	64.4	57.8	6.6
	Mexican Highland	424	61.3	81.7	47.8	33.9	61.2	62.3	60.2	2.1
	Middle Cascade Mountains	184	84.9	100.4	49.4	51.0	84.8	90.4	79.1	11.3
Pacific Border	Southern Cascade Mountains	189	55.7	68.2	50.2	18.0	55.7	57.7	54.1	3.6
	Sierra Nevada	701	65.3	95.3	46.0	49.3	65.3	65.8	64.7	1.1
	Oregon Coast Ranges	122	57.0	57.2	56.8	0.4	57.0	57.2	56.8	0.4
Lower Californian	Klamath Mountains	461	68.1	98.8	49.3	49.5	68.1	69.8	66.8	3.0
	California Trough	512	67.7	95.3	44.4	50.9	67.7	69.7	65.7	4.0
	California Coast Ranges	816	60.7	94.5	37.3	57.2	60.7	61.6	59.6	2.0
Middle Rocky Mountains	Los Angeles Ranges	338	67.1	96.2	38.0	58.2	67.1	68.2	65.8	2.4
	-	76	64.9	80.2	44.3	35.9	65.2	71.5	56.4	15.1
	-	214	57.0	62.2	48.0	14.2	57.0	59.7	54.1	5.6

Table 1. LAB depth characteristics by physiographic province.

Physiographic Province	Physiographic Section	Average Amplitude	Average Bootstrapped Amplitude _B
Columbia Plateau	Walla Walla Plateau	0.11	0.11
	Payette	0.08	0.08
	SNAKE RIVER PLAIN	0.09	0.09
	Harney	0.09	0.09
Colorado Plateau	High Plateaus of Utah	0.06	0.06
	Grand Canyon	0.10	0.10
	Navajo	0.09	0.09
Basin and Range	Great Basin	0.08	0.08
	Sonoran Desert	0.06	0.06
	Salton Trough	0.05	0.05
	Mexican Highland	0.07	0.07
Cascade-Sierra Mountains	Middle Cascade Mountains	0.07	0.07
	Southern Cascade Mountains	0.05	0.05
	Sierra Nevadas	0.06	0.06
Pacific Border	Oregon Coast Ranges	0.10	0.10
	Klamath Mountains	0.07	0.06
	California Trough	0.04	0.04
	California Coast Ranges	0.06	0.06
	Los Angeles Ranges	0.04	0.04
Lower Californian	-	0.06	0.06
Middle Rocky Mountains	-	0.06	0.06

Table 2. LAB average amplitudes by physiographic province.

	Box Half-Width (°)	Unbootstrapped Values				Bootstrapped Values			
		Average Depth (km)	Maximum Depth (km)	Minimum Depth (km)	Depth Range (km)	Average Depth (km)	Maximum Depth (km)	Minimum Depth (km)	Depth Range (km)
Control [41°N, -114°E]	0.1	72.0	78.4	68.6	9.8	71.9	78.4	68.6	9.8
	0.25	70.7	90.1	41.5	48.6	70.6	77.1	63.9	13.2
	0.5	75.8	90.3	41.5	48.8	75.9	79.3	73.0	6.3
	0.75	76.8	106.0	41.5	64.5	76.8	79.0	74.4	4.6
Lassen Volcanic Center [40.492°N, -121.508°E]	0.1	52.0	52.2	51.7	0.5	52.0	52.2	51.7	0.5
	0.25	51.8	53.1	50.2	2.9	51.8	52.3	51.0	1.3
	0.5	52.3	58.7	46.3	12.4	52.2	53.1	51.3	1.8
	0.75	55.3	71.0	46.0	25.0	55.3	56.8	54.2	2.6
Mammoth Mountain [37.197°N, -119.029°E]	0.1	70.7	71.5	69.9	1.6	70.7	71.5	70.1	1.4
	0.25	70.0	72.8	59.8	13.0	70.0	71.2	68.7	2.5
	0.5	68.3	73.0	59.2	13.8	68.2	69.3	67.3	2.0
	0.75	66.9	73.4	55.0	18.4	66.9	67.9	66.0	1.9
Salton Buttes [33.197°N, -115.616°E]	0.1	73.9	74.1	73.8	0.3	73.9	74.1	73.8	0.3
	0.25	70.0	75.0	36.6	38.4	70.0	74.4	62.6	11.8
	0.5	60.7	78.9	36.7	43.2	60.5	65.8	55.9	9.9
	0.75	57.1	80.1	36.7	43.4	57.1	59.8	54.4	5.4

Table 3. LAB depth characteristics for volcanic regions.